Energy & Environmental Science

ROYAL SOCIETY OF CHEMISTRY

PAPER

View Article Online
View Journal | View Issue

Cite this: *Energy Environ. Sci.*, 2026, **19**, 1215

Thermal decomposition pathways and interfacial reactivity in potassium-ion batteries: focus on the electrolyte and anode

Siddhartha Nanda,[a] Andrei Dolocan,[a] Ayrton Yanyachi,[b] Saurabh Sandip Satpute,[c] Doosoo Kim,[a] Kami L. Hull,[c] Donal Finegan,[d] Ofodike Ezekoye[b] and Hadi Khani *[ab]

Potassium (K)-ion batteries are an attractive alternative to lithium-ion batteries due to their resource abundance, graphite-anode compatibility, manufacturability, and reduced reliance on critical metals. However, their thermal safety remains poorly defined. Here, we investigate a widely accepted "safer" anode–electrolyte pair, a graphite anode with a low-flammable electrolyte, 2.5 M potassium bis(fluorosulfonyl)imide (KFSI) in triethyl phosphate (TEP), to clarify decomposition pathways and interfacial reactivity. This work shows that stand-alone TEP primarily volatilizes, whereas in the presence of KFSI it thermally decomposes *via* FSI-derived intermediates, producing exothermic reactions totaling ~264 J g^{-1} above 200 °C and generating organophosphate/fluorophosphate species (*e.g.*, diethyl fluorophosphate) together with SO_2, HNO_3, and SOF_2. This is roughly twice the heat released by a conventional $LiPF_6$-based carbonate electrolyte, underscoring that low flammability does not equate to safety. With potassiated graphite (KC_8), potassium leaching at ~63–80 °C triggers an early interfacial exotherm that builds an inorganic-rich secondary SEI and temporarily suppresses further anode attack up to ~200 °C. Beyond this temperature, electrolyte and anode–electrolyte reactions contribute a total of ~262 J g^{-1}, which is lower than that of the Li-ion analogue (~431 J g^{-1}) but occurs at an earlier onset (~65 *vs.* ~100 °C). Interfacial analysis shows that heating transforms the initially stratified SEI into a K-rich, chemically homogenized interphase. Our findings demonstrate that low flammability alone does not ensure thermal safety; rather, interfacial reactivity governs risk. Engineering the SEI composition, controlling salt–solvent coordination, and selecting suitable binders are essential for suppressing sub-100 °C reactivity while maintaining electrochemical performance.

Received 14th November 2025,
Accepted 19th January 2026

DOI: 10.1039/d5ee06908d

rsc.li/ees

Broader context

Potassium-ion batteries (KIBs) are gaining attention as a sustainable alternative to lithium-ion batteries (LIBs) because potassium is earth-abundant and supports low-cost, large-scale energy storage. However, despite advances in electrochemical performance, their thermal safety remains poorly understood, which is a critical barrier to commercialization if not addressed. A widely studied electrolyte, 2.5 M potassium bis(fluorosulfonyl)imide in triethyl phosphate solvent, is often presumed to enhance safety due to its low flammability and its ability to form an inorganic-rich, more thermally stable solid–electrolyte interphase than those formed in conventional carbonate-based electrolytes. We show that although less flammable, this electrolyte releases nearly twice the heat of a conventional carbonate-based LIB electrolyte and exhibits early-onset interfacial reactions with potassiated graphite under thermal stress. This work provides a comprehensive, mechanism-resolved analysis of electrolyte decomposition pathways and anode–electrolyte interactions in KIBs, revealing that safety risks stem from salt-solvent chemistry and anode–electrolyte interfacial reactivity rather than from bulk flammability. These insights redefine design priorities for next-generation batteries by emphasizing strategies to suppress sub-100 °C interfacial reactions and to engineer thermally resilient interfaces. Such advances are essential for enabling safe, high-performance KIBs that meet global energy storage demands while reducing dependence on scarce lithium resources.

[a] *Materials Science & Engineering Program and Texas Materials Institute, The University of Texas at Austin, Austin, Texas 78712, USA. E-mail: hadi.khani@austin.utexas.edu*
[b] *Walker Department of Mechanical Engineering, The University of Texas at Austin, Austin, TX 78712, USA*
[c] *Department of Chemistry, The University of Texas at Austin, Austin, TX 78712, USA*
[d] *National Laboratory of the Rockies, Golden, CO, USA*

1. Introduction

Potassium-ion batteries (KIBs) are gaining momentum as a sustainable alternative to lithium-ion batteries (LIBs) because potassium is more earth-abundant ($\sim$250 billion tons globally, compared to $\sim$89 billion tons for lithium) and more evenly distributed geographically.[1] Unlike sodium-ion batteries (SIBs), which exhibit limited Na^+ intercalation into graphite ($\sim$35 mAh g^{-1}), KIBs uniquely benefit from the ability of K^+ ions to reversibly intercalate into graphite, forming the stage-one KC_8 phase with a theoretical capacity of 279 mAh g^{-1} at an average potential of $\sim$0.1 V *vs.* K^+/K.[1,2] This potential is approximately 0.2 V lower than that of the Na^+/Na redox couple, enabling higher full-cell operating voltages when K-based anodes are paired with the same cathode chemistry.[3] Taken together, the abundance of potassium, the favorable anode potential, and the high intercalation capacity position KIBs as a particularly compelling candidate among next-generation rechargeable battery technologies.[4] KIB research has progressed markedly since the initial 2004 report of Prussian blue cathodes and the 2015 demonstration of reversible K^+ intercalation into graphite (KC_8);[5,6] however, the safety of KIBs remains a critical knowledge gap to this day. Historical precedent with LIBs emphasizes the importance of safety-focused design; although lithium cobalt oxide (LCO) was reported by John B. Goodenough's group in 1980, commercial LIBs did not arrive until Sony's 1991 launch, enabled by the replacement of lithium-metal anodes with carbonaceous anodes and by electrolyte formulations that improved stability and safety through the formation of a protective solid–electrolyte interphase (SEI) on carbon.[7,8] A similar trajectory could unfold with KIBs if the safety risks, particularly under thermal abuse, are not systematically understood and mitigated.[9]

One of the primary safety concerns in LIBs arises from the coupled reactivity of the intercalated graphite anode and the organic carbonate electrolyte, both of which drive key exothermic steps toward thermal runaway.[10,11] Upon heating, the SEI formed on lithiated graphite (LiC_6) begins to decompose, often as early as 80–120 °C, exposing highly reducing surfaces and triggering parasitic reactions with the electrolyte.[12] By about 200 °C, thermal decomposition of the salt, solvent, binder, and electrode components produces flammable and toxic gases such as CO, H_2, HF, and POF_3, increasing cell pressure and accelerating reactivity.[13,14] The thermal stability of lithiated graphite is therefore central to these events and has been investigated extensively by calorimetry and evolved-gas analysis.[15–17] Despite early theoretical predictions that LiC_6 is thermodynamically stable up to 250–330 °C, experimental evidence suggests that SEI degradation can trigger LiC_6 decomposition and Li leaching as low as 40 °C.[18] This observation further emphasizes the importance of studying the thermal stability of the anode and SEI. In addition to intercalated graphite and the SEI, the high flammability of conventional $LiPF_6$/EC/DEC electrolytes exacerbates thermal safety risks, prompting intense research into flame-retardant alternatives such as organophosphates including triethyl phosphate (TEP), trimethyl phosphate (TMP), dimethyl methyl phosphonate (DMMP), and tris(2,2,2-trifluoroethyl)phosphite (TTFEP).[19,20] A prior study reported the thermal behavior of non-flammable electrolytes (2.6 M LiFSI in TMP–TTFEP (1.00 : 1.67 by wt) and 2.6 M LiFSI in TMP–EC–TTFEP (1.00 : 0.09 : 1.67 by wt)) when combined with lithiated graphite and concluded (perhaps counterintuitively) that non-flammability does not ensure battery-level safety.[21] Instead, they observed that such electrolytes can react more violently with lithiated graphite than conventional carbonate electrolytes, emphasizing that the interfacial chemical reactivity at the electrode–electrolyte interface is the dominant factor dictating thermal risk. While LIBs have benefited from decades of safety-focused materials innovation, comparable systematic investigations are almost nonexistent in KIB systems. To the best of our knowledge, only one prominent study reported the thermal behavior of potassiated graphite with KPF_6-based carbonate electrolyte using differential scanning calorimetry (DSC).[22] In that study an exothermic onset was observed near 100 °C, attributed to reactions between fully potassiated graphite (KC_8) and a carbonate electrolyte.

Recently, KFSI in TEP has been explored as an alternative electrolyte to KPF_6 in EC/DEC because the KFSI-TEP electrolyte system is less flammable and promotes a more stable, inorganic-rich SEI on graphite than the predominantly organic SEI formed with KPF_6 in EC/DEC.[23] However, achieving stable passivation in phosphate-based electrolytes is often concentration sensitive. Although TEP is attractive from a safety standpoint due to its low flammability and high boiling point, prior studies show that dilute salt formulations contain a high fraction of "free" solvent molecules, which preferentially undergo reduction and form a non-uniform, weakly passivating interphase, resulting in poor electrochemical reversibility.[24] At high KFSI concentrations (*e.g.*, 2.5 M), the KFSI–TEP electrolyte also demonstrates significantly improved electrochemical performance (*e.g.*, a high coulombic efficiency of 99.6% for over 500 cycles) relative to both lower KFSI concentrations (*e.g.*, 1 M) and the conventional KPF_6–EC/DEC electrolyte.[23] However, the thermal behavior of the KFSI–TEP electrolyte, particularly in contact with potassiated graphite, has not been systematically evaluated. This gap motivates a detailed investigation of thermal behavior and evolved-gas release for KFSI-TEP with graphite anodes.

In this study, we systematically investigate the thermal decomposition and gas-release behavior of KIBs with graphite anodes using a widely studied low-flammable electrolyte: 2.5 M KFSI in TEP. A multi-modal analytical workflow, including TGA-DSC coupled with electron-ionization mass spectrometry (EI-MS) and Fourier transform infrared spectroscopy (FTIR), high-pressure DSC (HP-DSC), gas chromatography-mass spectrometry (GC-MS), and liquid chromatography (LC), is employed to correlate the mass loss, heat flow, and the evolution of gas-, solid-, and liquid-phase products with underlying decomposition pathways. We adopt a bottom-up approach, beginning with the analysis of individual components and progressing to binary and ternary mixtures to elucidate

decomposition mechanisms across various states of charge (SOCs). Bulk (*e.g.*, XRD) and surface (*e.g.*, TOF-SIMS, Raman, and XPS) characterization of electrodes at different SOCs and temperatures, combined with evolved-gas analysis, reveals how the SEI and electrolyte composition influence thermal stability and gas evolution. Our results show that intermolecular chemical interactions and coupled thermal reactions in binary (salt + solvent) and ternary (salt + solvent + electrode) systems can drive substantial gas evolution and self-heating, a behavior not captured when testing individual components in isolation. These insights highlight the need for safety assessments in next-generation KIBs and clarify which safety principles from LIBs are applicable to potassium-based systems and which require fundamental reevaluation.

2. Results and discussion

2.1. Thermal behavior of electrolyte

We first conducted thermal and gas characterization of the electrolyte (2.5 M KFSI in TEP) to develop a comprehensive understanding of the individual and combined thermal and gas release behaviors of KFSI, TEP, and their 2.5 M KFSI-TEP mixtures. This approach provides critical baseline information that later helps us identify the sources of reactions when the electrolyte interacts with the anode. To investigate the thermal behavior of the electrolyte and its components, two complementary thermal analysis techniques were employed: (i) TGA-DSC, using an aluminum crucible that is hermetically sealed in a glovebox and automatically pierced by a robotic system immediately prior to measurement. This setup prevents sample exposure to ambient conditions before analysis while allowing evolved gases to be captured and analyzed by MS and FTIR through the pierced hole (refer to Fig. S1a for the detailed working principle). (ii) HP-DSC using gold-plated stainless-steel crucibles that are hermetically sealed with a threaded cap, enabling precise measurement of heat release in a fully closed system that more closely mimics the pressure conditions within actual battery cells. Given that results from TGA-DSC or HP-DSC measurements can vary due to subtle differences in mass loading, sample inhomogeneity, crucible-sample contact, sample positioning, and crucible sealing or piercing, we implemented a repetition protocol to ensure reproducibility (see Fig. S1b). Particular attention was given to the consistency of onset temperatures, peak temperatures, and heat-flow signals across repeated measurements.

As shown in Fig. 1a, the DSC (from DSC-TGA measurements) of KFSI salt exhibits an endothermic peak starting at 102 °C (onset) and peaking at 108 °C. Since the onset temperature is typically taken as the melting point for pure inorganic substances,[25] 102 °C is assigned to the melting point of KFSI salt.[26,27] The onset temperature for thermal decomposition of KFSI is observed at 280 °C, followed by multiple decomposition events with peaks at 305 °C, 360 °C, 416 °C, 483 °C, and 570 °C, indicating a multistep decomposition process involving KFSI and its subsequent decomposition products. The total heat release and mass loss of the electrolyte, TEP, and KFSI are summarized in Table 1. For comparison, a previous report on the thermal stability of LiFSI showed a melting temperature of 145 °C and a peak thermal decomposition temperature of 330 °C, with a total mass loss of 31% by 500 °C.[28] In contrast, our TGA measurements indicate a significantly higher total mass loss of 50% for KFSI salt by 500 °C, with no additional mass loss between 500 and 600 °C (Fig. S2). To further investigate the decomposition products, we performed Raman spectroscopy at two different spots on the residual sample collected after the TGA-DSC measurements, in which the sample had been heated to 600 °C. As shown in Fig. S3a, the Raman spectra exhibit characteristic peaks at (i) 448 cm^{-1}, (ii) 666 cm^{-1} and 1001 cm^{-1}, and (iii) 153 cm^{-1}, 221 cm^{-1} and 473 cm^{-1}, corresponding to K_2S_2, $K_2S_2O_3$, and polymerized sulfur species (S_x), respectively.[29,30] In addition, the pale-yellow color of the residual powder observed after thermal decomposition (Fig. S3b) is characteristic of potassium-sulfur species (K_xS_y).[31] The TGA-DSC profile for TEP solvent, shown in Fig. 1a, displays a sharp endothermic peak at 219 °C, corresponding to the boiling and evaporation of TEP. The 100% weight loss confirms complete solvent evaporation, with no indication of decomposition or formation of residual solid byproducts (Fig. S2). The DSC curve of the electrolyte (Fig. 1a) shows multiple endothermic and exothermic peaks, which likely result from competing processes: the endothermic boiling and decomposition of TEP and the exothermic decomposition of the KFSI salt. The thermal decomposition of TEP is considered endothermic, as cleavage of the P–O–C bonds requires energy input, with volatilization further absorbing heat; this behavior is consistent with that of TMP, which has a similar phosphate ester structure.[32] Due to these competing reactions, the net heat release for the electrolyte is measured to be −219 J g^{-1}, as summarized in Table 1. A total weight loss of approximately 82% was observed for the electrolyte, leaving around 18% black solid residue (Fig. S2 and S3d). Raman analysis of this black residue (Fig. S3c) primarily indicates a carbon-rich composition, with no observable signals for potassium–sulfur species (K_xS_y), likely due to their low concentration in the solid. This carbonaceous material suggests that TEP, as the sole carbon source in the electrolyte, underwent thermal decomposition in the presence of KFSI. The details of individual thermal events are discussed in the following section.

While the TGA-DSC profiles provide critical insights into heat flow and mass loss, a comprehensive understanding of the decomposition mechanisms requires complementary gas-phase analysis. Accordingly, we conducted MS and FTIR analyses of the evolved gases during the thermal decomposition of both KFSI and the electrolyte. These analyses enabled the identification of gaseous species released at different temperatures, providing critical information to elucidate the underlying decomposition pathways. Evolved gas analysis by MS as a function of temperature from the decomposition of KFSI salt during TGA-DSC experiments is shown in Fig. S4a. The detected gases include HNO_3 (m/z = 63), SO_2 (m/z = 64), and SOF_2 (m/z = 86), which are released within the temperature range of 300 °C

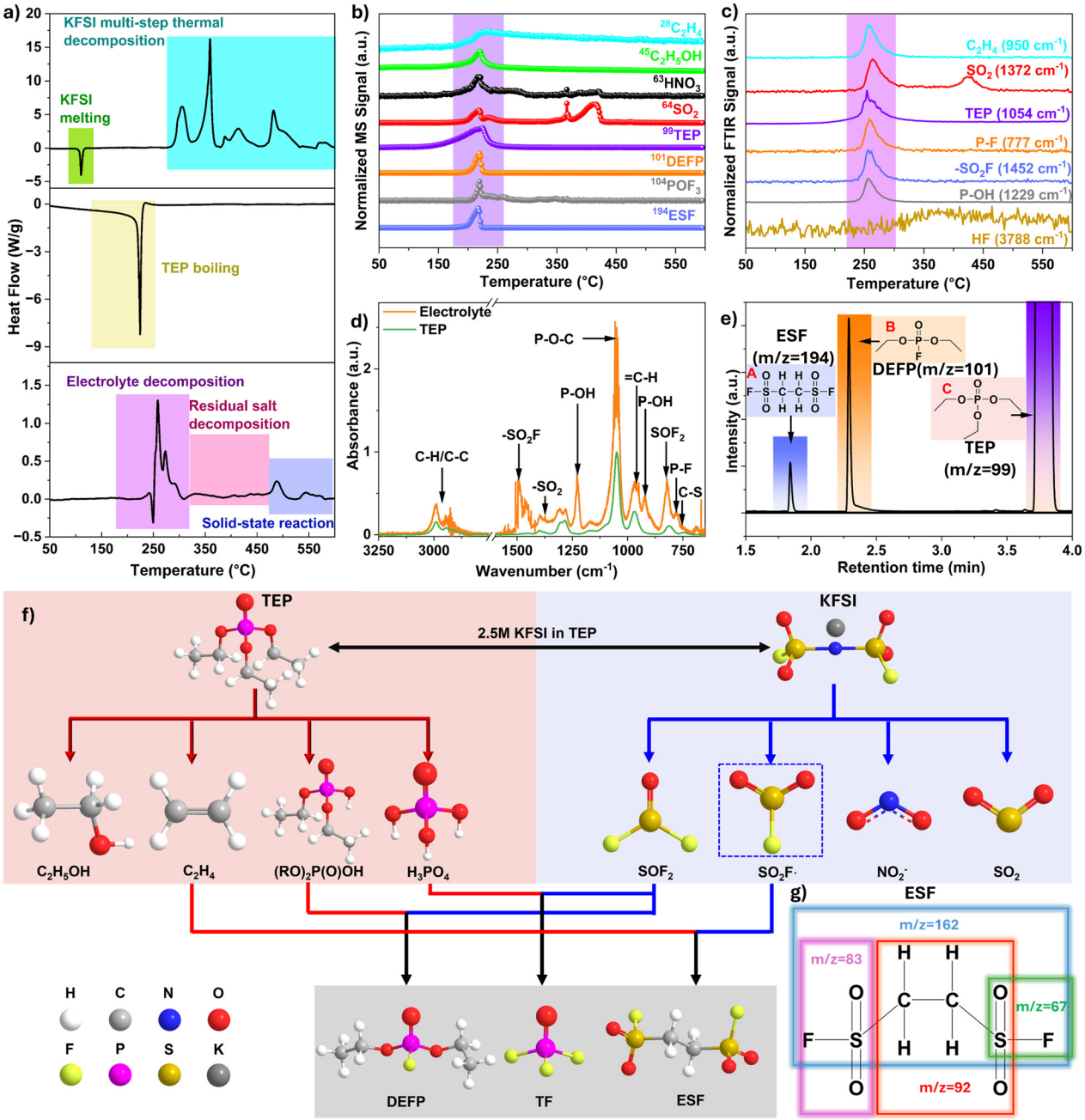

Fig. 1 (a) DSC profiles of KFSI (top), TEP (middle), and electrolyte (2.5 M KFSI in TEP - bottom); (b) *in situ* EI-MS signals and (c) FTIR spectra of gases evolved from the electrolyte during heating; (d) full FTIR spectrum at 250 °C for the electrolyte and TEP; (e) GC-MS chromatogram of the electrolyte after thermal treatment at 250 °C showing three main products; (f) proposed thermal decomposition mechanisms for the electrolyte; (g) fragmentation products of ESF.

Table 1 Total heat and the corresponding mass loss of electrolyte components measured between 25 and 600 °C. Negative values denote net exothermic heat release, while positive values denote net endothermic heat absorption. The total heat is calculated as: total heat = exothermic heat release + endothermic heat absorption

Sample	Total heat (J g^{-1})	Overall weight loss (%)
2.5 M KFSI in TEP	−219 (±10%)	82.0
TEP	+520 (±5%)	99.5
KFSI	−3290 (±3%)	48.5

to 500 °C, as indicated by the shaded yellow region in Fig. S4a. In Fig. S5, the MS spectrum shows the relative intensity of evolved gases plotted against *m/z* at 377 °C, the temperature corresponding to the maximum gas evolution. The signal at *m/z* = 64 dominates, indicating that SO_2 is the primary gaseous product released during the exothermic reaction at this temperature. In comparison, other gases such as SOF_2 and HNO_3 are detected at lower intensities, with their maxima occurring slightly below 377 °C, as confirmed by both MS and FTIR

analyses (Fig. S4a and b). Previous studies on the thermal decomposition of LiFSI have reported the evolution of gases such as NO_2 and SO_2 under similar conditions.[20] The FTIR analysis of KFSI decomposition (Fig. S4b) also confirms the release of HNO_3, SO_2, and SOF_2 gases within the same temperature range (300–500 °C). The full FTIR spectrum recorded at 377 °C (Fig. S4c) shows a peak at 1256 cm^{-1} corresponding to NO_3^-, attributed to asymmetric N–O stretching vibrations, supporting the presence of the HNO_3 gas,[33] which was also detected by MS. Strong, intense peaks observed at 1300–1450 cm^{-1} and at 1150 cm^{-1} provide clear evidence of SO_2 release.[34] Additionally, a weak peak at 808 cm^{-1} is characteristic of the S–F symmetric stretching in SOF_2 gas.[35] A series of rotational bands spanning 4300–3600 cm^{-1} are characteristic of vapor-phase hydrofluoric acid (HF), indicating HF release;[36,37] however, HF was not detected by MS, likely because its concentration was below the MS detection limit. The enlarged FTIR region highlighting these characteristic bands is presented in Fig. S4d.

Based on the combined results from TGA-DSC, MS, FTIR, and Raman analyses, the thermal decomposition of KFSI can produce gaseous products such as NO_2, SO_2, and SOF_2, along with solid residues including K_2S_2, $K_2S_2O_3$, and polymerized sulfur species (S_x). Subsequent secondary reactions with trace moisture convert NO_2 (quantitatively) and SOF_2 (partially) to HNO_3 and HF + SO_2, respectively.[38] Similar behavior has been observed in the thermal decomposition in LIBs, where $LiPF_6$ salt decomposes at approximately 206 °C to produce PF_5, which readily hydrolyzes in the presence of trace moisture to generate HF.[39]

The identification of evolved gases from the decomposition of the electrolyte using TGA-DSC-MS and TGA-DSC-FTIR was somewhat challenging due to detector saturation caused by the intense signals from TEP solvent peaks. Therefore, to reduce the concentration of TEP vapor reaching the detector at any given time and to improve the resolution of gas detection in the electrolyte experiments, TGA-DSC was performed at a reduced heating rate of 2 °C min^{-1}. As a result, the onset of gas release was observed at a lower temperature (see the TGA profile differences in Fig. S6). Fig. 1b presents the MS thermogram, showing the major gases evolved from the electrolyte as the temperature was ramped from 40 °C to 600 °C. To better illustrate gas identification, mass spectra recorded at five selected temperatures (200, 210, 220, 230, and 240 °C) are shown in Fig. S7. These temperatures were chosen because they capture most electrolyte-derived gas release and the evolution patterns of the main species. The main peaks observed include m/z = 64 (corresponding to SO_2), m/z = 99 and 155 (major fragment ions of TEP), m/z = 101, and m/z = 194. Notably, the intensity of the m/z = 101 peak changes simultaneously with peaks at m/z = 113 and m/z = 129, and their intensity ratio remains constant at approximately 1 (101) : 0.34 (113) : 0.26 (129) throughout the heating profile. This observation is consistent with the previously reported MS spectrum for diethyl fluorophosphate (DEFP),[40] supporting the assignment of m/z = 101 to a characteristic fragment of DEFP. Another major peak was observed at m/z = 194, accompanied by characteristic fragment ions at m/z = 92, 83, 67, and 162. The presence of a small peak at m/z = 196, which can be attributed to the S^{34} isotope, together with the assignment of m/z = 83 and 67 to SO_2F^+ and SOF^+, respectively, supports the identification of this compound as ethane-1,2-disulfonyl difluoride (ESF), which has been previously reported as an independent, stable species.[41,42] Additionally, a weak peak at m/z = 104 is consistent with phosphoryl fluoride or TF (POF_3), as confirmed by the presence of its fragment ions at m/z = 85 (POF_2^+) and m/z = 69 (PF_2^+). The two other major gases, ethanol (C_2H_5OH, m/z = 45) and ethylene (C_2H_4, m/z = 28), are generated from the thermal decomposition of TEP.[43] An enlarged MS profile between 150–250 °C for m/z = 99 (TEP's fragment ion), m/z = 28 (ethene), and m/z = 111 is shown in Fig. S8a. The main fragment ions of diethyl phosphate ($(C_2H_5O)_2P(O)OH$, DEP) appear at m/z = 65, 83, and 111.[44] To elucidate the decomposition behavior of TEP and DEP, we monitored the evolution of fragment ion m/z = 111, which is common to both species. Initially, the signal at m/z = 111 overlaps with m/z = 99, consistent with TEP fragmentation up to 210 °C. However, between 210–220 °C, the intensity of m/z = 111 as well as m/z = 28 (ethene) increases, while that of m/z = 99 decreases, indicating the decomposition of TEP to DEP. Importantly, neat TEP alone does not generate decomposition gases but instead evaporates completely, as evidenced by the endothermic event in Fig. 1a and the overlapping MS profiles for m/z = 99 and 111 in Fig. S8b. This observation emphasizes the catalytic role of KFSI in promoting TEP decomposition. As shown by the MS signal trends of DEP (m/z = 111), DEFP (m/z = 101), SOF_2 (m/z = 86), and POF_3 (m/z = 104) in Fig. S8c, once DEP forms it reacts with SOF_2, produced from salt decomposition, to generate DEFP and POF_3 (see the schematic in Fig. S8d). Furthermore, the early release of HNO_3 (m/z = 63) and SO_2 (m/z = 64) between 200 and 250 °C in the electrolyte (Fig. 1b), compared to their evolution above 300 °C in the KFSI salt alone (Fig. S4a and b), highlights differences in the thermal decomposition pathways for the electrolyte and salt.

To further validate these results, we conducted a series of complementary experiments, including TGA-DSC-FTIR analysis of the evolved gases and GC-MS analysis of the thermally decomposed electrolyte. Fig. 1c presents the FTIR thermogram showing the major gaseous species detected from the electrolyte as the temperature was ramped from 40 °C to 600 °C. To more clearly demonstrate the gas identification process, FTIR spectra for the electrolyte and pure TEP recorded at 250 °C are shown in Fig. 1d. The FTIR spectrum of the electrolyte at 250 °C shows a peak around 950 cm^{-1}, assigned to ethylene (C_2H_4), which was also detected in the MS spectrum at the same temperature (Fig. 1b).[45] A strong peak at ~777 cm^{-1} corresponds to P–F stretching vibrations, suggesting the possible release of DEFP and/or POF_3, both of which were also identified in our MS results (Fig. 1b).[46] Two distinct, sharp peaks at 923 cm^{-1} and 1229 cm^{-1}, observed only in the electrolyte spectrum, are attributed to δ(P–OH) and ν(P–OH) vibrations, respectively.[47,48] These vibrational signatures support the release of phosphorus-containing species with –OH

functionalities, such as DEP and H_3PO_4, which form *via* thermal decomposition of TEP, as previously reported.[49] The peak at 1372 cm^{-1} (absent in TEP's FTIR) indicates the release of SO_2 gas. The electrolyte's FTIR spectrum shows several additional peaks in the 1400–1550 cm^{-1} region, which are absent in the TEP spectrum (Fig. 1d and Fig. S9), indicating the presence of additional gases whose characteristic vibrations fall within this wavenumber region. Specifically, the twin peaks at 1436 and 1448 cm^{-1} further confirm the presence of ethylene gas,[40,50] while a series of peaks between 1450 and 1550 cm^{-1}, including a characteristic peak at 1504 cm^{-1}, have been previously assigned to $-SO_2F$-containing compounds.[51] The broad absorption peaks between 2800 and 3200 cm^{-1}, which are also observed for TEP, are assigned to C–H vibrations from alkyl groups.[52] Additionally, a small shoulder peak in the electrolyte's FTIR spectra at 760 cm^{-1} has been previously assigned to C–S stretching vibrations originated from sulfonate compounds.[53] Collectively, these vibrational signatures corresponding to $-SO_2F$, C–H and C–S groups in the FTIR spectrum of electrolyte at 250 °C further support the EI-MS observation of ESF (m/z = 194) as a decomposition product during thermal breakdown of the electrolyte. Additionally, HF evolution was confirmed by the appearance of FTIR peaks at 3788 cm^{-1}, with continuous release starting above 250 °C. The FTIR peak for SOF_2 at 810 cm^{-1} is not discussed here as it overlaps with a characteristic TEP peak in the same region.

We further performed GC-MS analysis on the products of thermally decomposed electrolyte (Fig. S10a and b). The chromatogram results revealed the presence of three primary compounds, all of which exist as liquids at room temperature, with retention times of 1.8 min, 2.3 min, and 3.7 min for gases A, B, and C, respectively (Fig. 1e). Database matching (Fig. S11) reveals a 100% match between product C and TEP, as well as between product B and DEFP, both of which are consistent with our earlier TGA-DSC-MS and TGA-DSC-FTIR analyses. In contrast, product A, characterized by a dominant fragment at m/z = 194, does not match any compound in the database. However, based on the fragmentation patterns observed in both TGA-DSC-MS and GC-MS (Fig. 1g), together with TGA-DSC-FTIR evidence indicating the presence of C–H, C–S and $-SO_2F$ functional groups, we propose that the product A is ESF, a major gaseous product formed during the thermal decomposition of 2.5 M KFSI in TEP.

To further understand the thermal decomposition behavior of 2.5 M KFSI in TEP, the fundamental solvation structure of this electrolyte system was investigated using Raman spectroscopy of the electrolyte and its individual components (Fig. S12a and b). The Raman modes can be assigned to the molecular vibrations of FSI^- and TEP as follows: the 680–780 cm^{-1} band corresponds to both S–N–S stretching vibrations in FSI^- and P–O–C stretching vibrations in TEP, the band at ~1100 cm^{-1} mainly originates from $-CH_3$ rocking vibrations in TEP, the band from 1200–1240 cm^{-1} accounts for S═O stretching vibrations, the bands between 1240 and 1330 cm^{-1} can be assigned to P═O stretching and $-CH_2$ twisting vibrations.[54] Previous studies have shown that fitting of the S═O Raman band can quantify free FSI^- anions, FSI^- in contact ion pairs (CIPs), and FSI^- in aggregates (AGGs).[54,55] Peak deconvolution was performed using a Voigt function, and the results indicate two major peaks: one at 1216 cm^{-1} corresponding to CIP-associated FSI^- (48%), in which one K^+ ion coordinates with a single FSI^- ion, and another at 1224 cm^{-1} corresponding to AGG-associated FSI^- (52%), in which one K^+ ion is coordinated by two FSI^- anions (Fig. S12c). Based on the Raman results, the proposed solvation structure is illustrated in Fig. S12d. This unique solvation environment, with AGG-associated FSI^- and CIP-associated FSI^- accounting for 52% and 48% of the species, respectively, and with virtually no free anions, implies strong electrostatic cation–anion interactions. Such intermolecular interactions polarize FSI^- anions, weaken the S–N bonds, and lower the LUMO energy, thereby making the anion more susceptible to homolytic S–N bond cleavage upon thermal activation, leading to the formation of $^{\bullet}SO_2F$ and $FO_2SN^{-\bullet}$ radicals ($FO_2SN^-SO_2F \rightarrow FO_2SN^{-\bullet} + {}^{\bullet}SO_2F$).[56]

Building on these experimental observations, the proposed decomposition mechanism for 2.5 M KFSI in TEP is schematically illustrated in Fig. 1f. The decomposition of TEP into alkyl phosphates (*e.g.*, DEP), phosphoric acid, ethylene, and ethanol is apparently triggered by radicals generated from KFSI decomposition, and such decomposition products of TEP have been previously reported.[43] This decomposition process is evidenced by the sharp endothermic peak observed at ~250 °C in the TGA-DSC profile of the electrolyte (Fig. 1a). Since unsaturated C═C bonds serve as favorable reaction sites for sulfonyl radicals,[56] fluorosulfonyl radicals can exothermically undergo radical addition reactions with ethylene, generated from the endothermic decomposition of TEP (TGA-DSC in Fig. 1a), leading to the formation of ESF. In parallel, the fluorination of DEP and phosphoric acid by highly reactive fluorine-containing species such as $NSO_2F^{\bullet}$ and SOF_2 likely results in the formation of DEFP and POF_3, respectively. The fluorination of DEP by SO_2F_2 to form DEFP has been previously reported.[57] This fluorination pathway is highly plausible given the presence of these reactive fluorine-containing species at elevated temperatures around 250 °C. Similar to the salt alone, the NO_2 and SOF_2 generated from FSI^- decomposition can further react with H_2O (resulting from DEP condensation or trace impurities) to generate HNO_3 and SO_2 + HF, respectively. These reactions collectively account for the large exothermic peaks observed between 250 and 300 °C in the TGA-DSC profile of the electrolyte (Fig. 1c).

2.2. Thermal behavior of the anode–electrolyte system

To evaluate how the degree of potassium intercalation in the graphite anode influences the thermal behavior of the anode–electrolyte (An + Ely), HP-DSC measurements were performed at three SOCs: 0% (2.50 V), 50% (~3.72 V), and 100% (4.30 V). The corresponding electrochemical performance of the full cell is shown in Fig. S13, with the full cell configuration detailed in the Experimental methods section. The HP-DSC measurements, with results presented in Fig. 2a, were conducted on anodes harvested from full cells after formation cycles at the

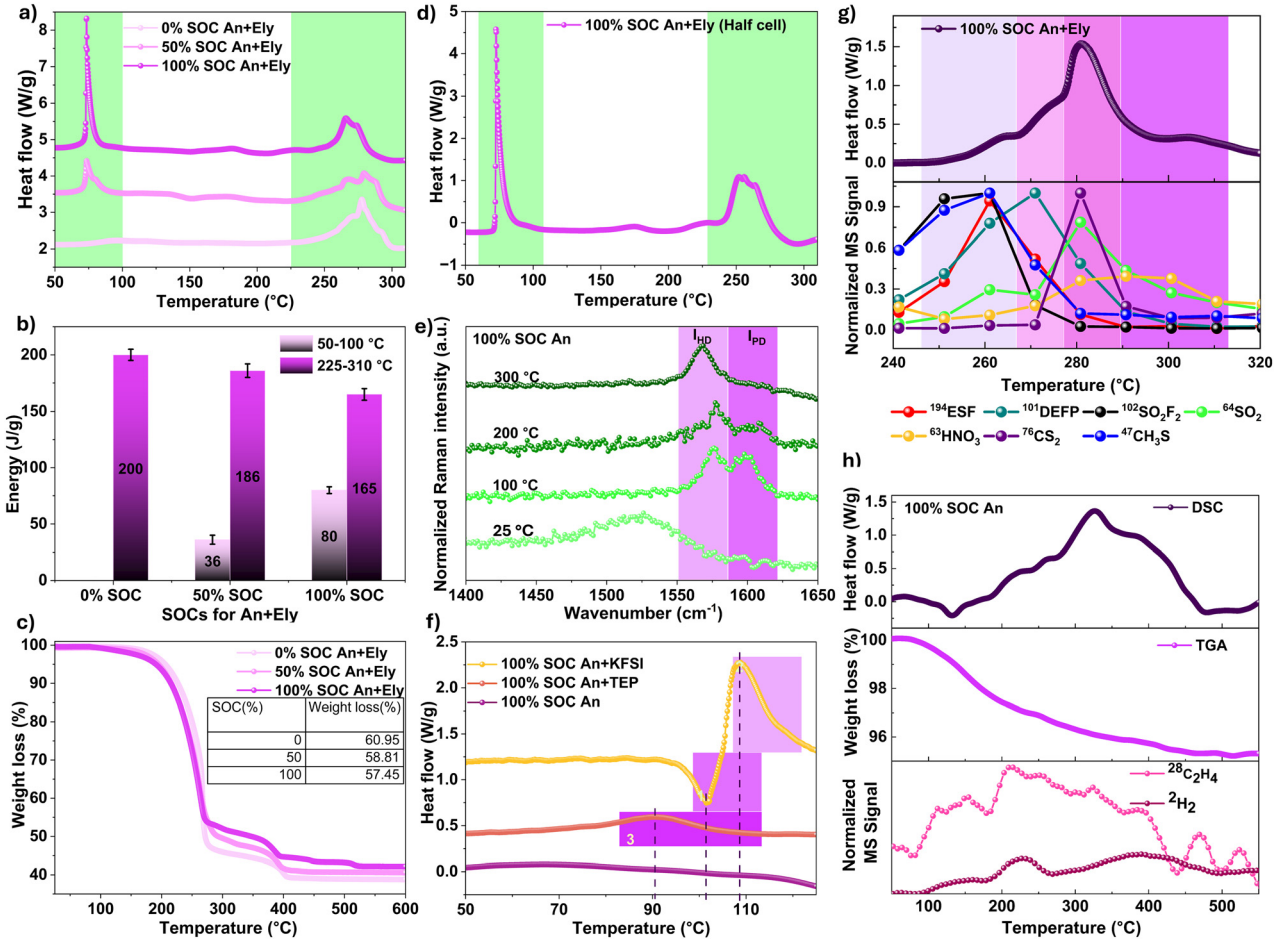

Fig. 2 (a) HP-DSC measurements of cycled anodes at 0%, 50%, and 100% SOC with electrolyte; (b) Calculated heat release (J g^{-1}) from HP-DSC in two different regions; (c) TGA weight loss (%) of cycled anodes at 0%, 50%, and 100% SOC with electrolyte; (d) HP-DSC of the cycled anode (100% SOC), retrieved from a half cell, with electrolyte; (e) *ex situ* Raman spectra of the 100% SOC anode at different temperatures; (f) controlled TGA-DSC measurements of the cycled anode alone, with KFSI salt, and with TEP solvent; (g) enlarged view for MS gas analysis for 100% SOC anode with electrolyte; (h) TGA-DSC-MS analysis of the 100% SOC anode without electrolyte.

specified SOCs. The anodes were washed with DMC to remove residual electrolyte, dried under an inert atmosphere at 25 °C, and subsequently mixed with fresh electrolyte at a 1 : 1 mass ratio of anode to electrolyte (see the Experimental methods section). The resulting HP-DSC profiles in Fig. 2a are divided into two characteristic temperature regions: region I, corresponding to low-temperature thermal events between 50 and 100 °C, and region II, which captures high-temperature thermal events in the range of 225 to 310 °C. The intermediate temperature region (100–225 °C) exhibited small exothermic events, accounting for approximately 15 J g^{-1}, are likely associated with the decomposition of binder and TEP-derived organic compounds, an assignment that will be further examined by gas analysis in the following section. The specific energy release (J g^{-1}) from the graphite anode and electrolyte in the low and high temperature regions, across all SOCs, is presented in Fig. 2b. The total energy evolved increased from 200 ± 5 J g^{-1} at 0% SOC to 245 ± 2 J g^{-1} at 100% SOC, indicating that heat release is dependent on the degree of potassiation. This trend is consistent with previously reported thermal behavior of lithiated graphite in contact with $LiPF_6$-based carbonate electrolytes in LIBs.[58] Notably, a sharp exothermic peak at ~75 ± 1 °C was observed for the 100% SOC anode with electrolyte, corresponding to an energy release of 80 ± 3 J g^{-1}. A similar but smaller exothermic feature was observed for the 50% SOC sample, with a heat release of 36 ± 4 J g^{-1}, while no exothermic peak was detected for the 0% SOC sample within region I. An opposite trend was observed in region II: with increasing SOC, the heat release decreased from 200 ± 5 J g^{-1} at 0% SOC to 186 ± 6 J g^{-1} and 165 ± 5 J g^{-1} at 50% and 100% SOC, respectively. TGA-DSC experiments were also performed on cycled anodes with electrolyte at 0% and 100% SOCs (Fig. S14a and Fig. 2c). For the 100% SOC anode–electrolyte sample, the exothermic peak at 78 ± 2 °C was consistently observed. Repeated DSC measurements confirmed that the onset temperature for exothermic reactions in fully potassiated graphite with 2.5 M KFSI in TEP is around 65.0 ± 0.1 °C, peaking at 78 ± 2 °C (Fig. S14b). In contrast, a previous study on potassiated graphite in contact with KPF_6-based organic carbonate electrolytes reported the first exothermic

peak at 100 °C, attributed to reactions between KC_8 and the electrolyte (0.8 M KPF_6 in EC/DEC, 1 : 1 by volume).[22] The onset temperature of thermal runaway is a critical parameter because earlier onset (lower temperature) accelerates cell heating and can trigger subsequent thermal events, ultimately leading to thermal runaway.[9] Our results show that the onset temperature of the exothermic reaction of the potassiated graphite anode with the low-flammable 2.5 M KFSI-TEP electrolyte is about 25–30 °C lower than that observed in the flammable 0.8 M KPF_6 EC/DEC electrolyte.

As the magnitude of heat release in region I and region II is inversely proportional, it suggests that the reactions in both regions involve the same reactants but are constrained by a fixed amount of reactant. The relevant reactants here are the electrolyte, SEI, and graphite at different degrees of potassiation. The increase in total heat with higher degrees of potassiation (*i.e.*, 0% *vs.* 100% SOC) indicates that reactions directly involving the SEI and electrolyte are unlikely to be the dominant source of heat in region I. This is because the electrolyte mass was kept constant at a 1 : 1 ratio with the cycled anode, and the inorganic-rich SEI is reported to be relatively stable with cycling.[59] Moreover, the absence of any exothermic event in region I for the 0% SOC anode–electrolyte sample further excludes the SEI–electrolyte reaction as the primary contributor. Instead, we propose that the reactions in region I arise from direct interactions between the electrolyte and the potassiated graphite anode. The TGA profiles at different SOCs (Fig. 2c) show only a slight decrease in mass loss, from 61.0% to 57.5%, as the SOC increases. Importantly, there is only slight mass loss (~0.37%, Fig. S14b) below 100 °C, where the first exothermic event is observed, indicating that the low temperature exotherm associated with reaction between the potassiated graphite anode and the electrolyte mainly produces solid products, which we refer to as a secondary interfacial layer.

To interpret the reactions occurring in these regions, we first refer to the well-established degradation mechanisms of thermally driven reactions involving lithiated graphite electrodes with and without electrolyte addition in LIBs, which have been extensively studied.[12,18,60,61] These reactions can be summarized as follows: below 170 °C, the exothermic events arise from thermally driven and electrolyte-catalyzed decomposition of organic SEI components, chemical reactions between SEI components and leached Li, and reductive decomposition of the electrolyte by lithiated graphite. This reductive decomposition continues and reaches a maximum (in terms of energy release) at 218 °C. In addition, the leached Li melts and reacts with the PVDF binder above 170 °C. Finally, the protective secondary SEI, formed due to electrolyte decomposition on lithiated graphite, decomposes at 240 °C, leading to electrolyte penetration into the graphite structure and subsequent exfoliation. Furthermore, in LIBs, O_2 released from the cathode reacts with the available electrolyte and can trigger thermal runaway.

The anode–electrolyte system of KIBs investigated in this study features two key differences compared to conventional LIBs. First, the potassiated graphite anode initiates earlier reactions with the electrolyte, SEI, and binder, concurrent with potassium leaching at comparatively low temperatures. Second, the electrolyte used here (2.5 M KFSI in TEP) is highly concentrated and non-carbonate-based, forming an inorganic-rich SEI that has been reported to exhibit higher thermal stability than the organic-rich SEI typically associated with carbonate-based electrolytes.[23]

To investigate possible catalytic contributions from Mn and Fe species dissolved from the Prussian blue cathode ($K_xMn[Fe(CN)_6]_{1-y}\square_y{\cdot}nH_2O$ where $\square$ represents vacancies) and subsequently deposited in the SEI (*e.g.*, Mn and Fe oxides/fluorides) during cycling,[62] HP-DSC measurements were performed on a 100% SOC potassiated graphite anode harvested from a half-cell assembled against K metal using the same electrolyte (Fig. 2d). The charge–discharge profile for this half-cell is shown in Fig. S15a. The DSC response closely matched that of the 100% SOC anode retrieved from full cells (Fig. 2a), confirming that Mn and Fe crossover from the cathode does not contribute to the observed exothermic events in the anode–electrolyte system.

To probe the temperature-dependent structural changes and assess the thermal stability of potassiated graphite (KC_8), *ex situ* confocal Raman experiments were performed on dry anode samples (at 100% SOC) subjected to heat treatment at different temperatures. The Raman spectra of the cycled, fully potassiated graphite anode sample heat-treated at 25, 100, 200, and 300 °C are shown in Fig. 2e. At 25 °C, the spectrum shows an asymmetric Fano-resonance shape due to interference between the metallic-like behavior of stage-I graphite intercalated compounds (GICs) and the resonant phonon scattering process, which is characteristic of KC_8 Raman scattering.[63] The formation of KC_8 was also evident from the bright yellow coloration of the sample (Fig. S15b). Upon thermal treatment to 100 °C, two distinct peaks appear at 1578 cm^{-1} (I_{HD}) and 1600 cm^{-1} (I_{PD}), corresponding to highly depotassiated (HD) and partially depotassiated (PD) regions, respectively. The I_{HD} peak originates from surface-localized deintercalated regions, suggesting K leaches from the surface of the graphite lattice upon thermal treatment, while the I_{PD} peak reflects stronger K–C interactions where K remains intercalated. The emergence of this Raman doublet highlights localized heterogeneity and the importance of hot spots during heating.[64] This behavior is consistent with previous observations for electrochemically lithiated graphite, where Li begins to leach out of the graphite structure above ~40 °C.[18] Upon further heating to 200 °C, the I_{PD} peak decreases as more surface K leaches out, and the I_{HD}/I_{PD} ratio increases to 1.17, corresponding to the formation of KC_{72}.[63] At 300 °C, the I_{PD} peak disappears entirely, leaving a single peak at 1570 cm^{-1}, indicative of graphite reformation on the surface beneath the SEI. These findings help explain the distinct thermal behavior of intercalated graphite with the electrolyte, though reaction with electrolyte may further promote K deintercalation into the bulk compared to what is observed in Raman results for dry potassiated graphite anodes. In LIBs, the exothermic event related to reduction of electrolyte by leached Li occurs only above 200 °C after the Li has melted. In contrast, the analogous graphite anode–electrolyte reaction

in K-intercalated graphite with 2.5 M KFSI-TEP electrolyte begins at a much lower temperature (~65 °C).

Fig. S16a shows XRD patterns of potassiated graphite anodes at 100% SOC for samples that were (i) washed and dried, and (ii) washed, dried, and heated at 110 °C. While *ex situ* Raman analysis reveals near-surface potassium leaching from intercalated graphite at ~100 °C, the KC_8 reflection in *ex situ* XRD remains unchanged after heating to 110 °C, indicating that the bulk structure remains intercalated. Thus, in the absence of electrolyte, potassium leaching is confined to the surface and is likely incorporated into the SEI (see the discussion on ToF-SIMS and XPS analysis).

To further investigate the thermally driven degradation mechanisms, a series of controlled experiments were conducted to isolate the individual contributions of KFSI, TEP, and the anode to the overall heat release observed in the anode–electrolyte system at 100% SOC. TGA-DSC measurements were performed on three additional samples: (i) fully (100% SOC) potassiated graphite anode in contact with TEP solvent, (ii) fully potassiated graphite anode with only KFSI salt present, and (iii) fully potassiated graphite anode after washing and drying. The DSC profiles focusing on the low-temperature region (50–125 °C) of the potassiated graphite anodes are shown in Fig. 2f, while full-range thermal profiles (25–600 °C) are provided in Fig. S16b. The DSC results indicate that the low-temperature exothermic peak observed for the 100% SOC anode–electrolyte sample is absent in the corresponding dry 100% SOC anode. This indicates that thermally driven interfacial reactions between potassiated graphite and the SEI or binder, which lead to surface potassium leaching (as confirmed by Raman), do not produce detectable heat-flow changes in the absence of electrolyte and therefore do not generate a distinct exothermic peak above the baseline in our DSC measurements. Taken together, these observations confirm that the observed low-temperature exothermic reaction arises from direct reaction between the electrolyte and the potassiated graphite anode.

The DSC thermogram of the 100% SOC potassiated graphite anode in contact with TEP exhibits an exothermic peak at 90 °C (27 J g^{-1}) (Fig. 2f), attributed to the reductive decomposition of TEP by the potassiated graphite anode. The DSC thermogram of the 100% SOC anode mixed with KFSI salt shows an initial endothermic peak at ~105 °C, corresponding to the melting point of KFSI, immediately followed by a strong exothermic peak, indicating a vigorous reaction between molten KFSI and the potassiated graphite anode (Fig. 2f). This observation highlights the dominant role of KFSI salt in driving the low-temperature exothermic peak observed near ~75 °C. It further suggests that at lower temperatures, a reaction between solid KFSI and the potassiated graphite anode is unlikely due to limited solid–solid contact and the presence of the SEI, which prevents direct interaction. However, in solution and in the molten state, KFSI can initiate exothermic reactions with the potassiated graphite anode at ~65 °C and ~105 °C, respectively. Overall, the KC_8/TEP and KC_8/KFSI control experiments distinguish the contribution of solvent- *versus* salt-driven reactions: while TEP can be directly reduced at the potassiated graphite surface, solvated or molten KFSI dominates interfacial reactivity at elevated temperatures.

To further investigate the mechanism of thermal events between potassiated graphite and the electrolyte, TGA-DSC analysis coupled with EI-MS was performed to identify the evolved gases over the temperature range of 25–600 °C (Fig. S17a). A very small amount of gas evolution was detected at the exothermic peak around ~75 °C, consistent with the TGA data showing 0.37% mass loss below 100 °C (Fig. 2c and Fig. S14b). The MS analysis shows the evolution of a small quantity of CO/C_2H_4 and H_2O gases in this region, indicating that the reaction in this region is predominantly driven by exothermic reduction of the FSI^- anion by the potassiated graphite anode, most plausibly yielding the formation of a secondary inorganic-rich layer *via* electrolyte reduction. The formation of such passivation layer on potassiated graphite at 75–80 °C is highly plausible because the substantial volume expansion (~61% for KC_8) during electrochemical potassiation induces mechanical stress and cracking in the SEI,[22] creating pathways for direct contact between the electrolyte and the KC_8 surface, and thereby predisposing the system to premature exothermic reactions at elevated temperatures (*e.g.*, 75 °C).[22] Above 100 °C, gas evolution becomes prominent, with key detected species including H_2 (m/z = 2), H_2O (m/z = 18), and CO/C_2H_4 (m/z = 28), attributed to reactions between the potassiated graphite anode with the CMC-based binder, removal of adsorbed and bound water from the binder (Fig. S17b), and thermal decomposition of inorganic–organic SEI components in the secondary interfacial layer, as discussed in the XPS section. Given the low binder fraction (~4 wt% in the anode and a binder-to-electrolyte mass ratio of ~0.08), its contribution to the total heat release of the composite is expected to be limited in the high temperature region. An enlarged view of the selected gases released in the high temperature region (240–310 °C) is shown in Fig. 2g. The major gases detected in this temperature region include CH_3SH (m/z = 47), CS_2 (m/z = 76), ESF (m/z = 194), DEFP (m/z = 101), SO_2F_2 (m/z = 102), SO_2 (m/z = 64), HNO_3 (m/z = 63), and DEP (m/z = 111). The integration of TGA, DSC, and Raman analyses with gas-phase composition data along with XPS and TOF-SIMS results (to be discussed later) supports the conclusion that the major exothermic events between 240 and 310 °C can be attributed to (i) electrolyte decomposition, (ii) reactions of potassiated graphite with binder and electrolyte, (iii) decomposition of inorganic–organic SEI components, and (iv) secondary gas-phase reactions between evolved intermediates. Regarding the latter, while establishing direct correlations between reactants (SO_2, SO_2F_2, CO/C_2H_4, DEP) and products (DEFP, ESF, CH_3SH, CS_2) is challenging due to further decomposition (*e.g.*, $SO_2F_2 \rightarrow SO_2$) and potential cross-reactivity, some mechanistic insights can still be inferred. For instance, CH_3SH and CS_2, which were not observed during standalone electrolyte decomposition, likely originate from reductive reactions between FSI-derived components (as sulfur sources) and the potassiated graphite anode, which serves as both carbon and electron donor, leading to S–C

bond formation. Similarly, product species such as ESF and DEFP may form *via* reactions of SO_2F_2, a decomposition product of KFSI, with TEP-derived organics such as C_2H_4 or DEP, respectively. The TGA-DSC-MS analysis of the 100% SOC anode without electrolyte (Fig. 2h) shows a total mass loss of ~4% over the complete heating range from 25 to 600 °C, with no detectable mass loss below 100 °C. The mass loss above 100 °C is accompanied by continuous exothermic peaks and the evolution of H_2 and CO/C_2H_4 gases, which are attributed to the reaction between the potassiated graphite anode and the binder and decomposition of the inorganic–organic components in the secondary interfacial layer. Similar gas release profiles have been reported for thermally treated, washed, and dried lithiated graphite anodes.[18]

Building on the findings from the thermal and gas release analyses of systems containing potassiated graphite, K metal, KFSI, TEP, and the electrolyte, in their individual, binary, and ternary combinations, we propose the following sequence of thermal events during heating from 25 to 600 °C, as illustrated in Fig. 3.

1. Low-temperature reactions (25–100 °C): a schematic representation of the potassiated graphite anode with an inorganic-rich SEI is shown in Fig. 3a. Thermal events in this region initiate when electrolyte components penetrate the SEI and react with the potassiated graphite beneath (Fig. 3b). The carbon layers in graphite contain low-energy empty orbitals (π^* antibonding orbitals) that accept electrons when K^+ electrochemically intercalates between the graphitic layers. Upon heating, the potassiated graphite becomes highly reducing and donates electrons to surrounding species such as KFSI, TEP, the binder, and the SEI, triggering their reduction. This process occurs concurrently with potassium deintercalation (*i.e.*, leaching) to maintain local charge neutrality. A comparable leaching process has been reported for Li^+ in lithiated

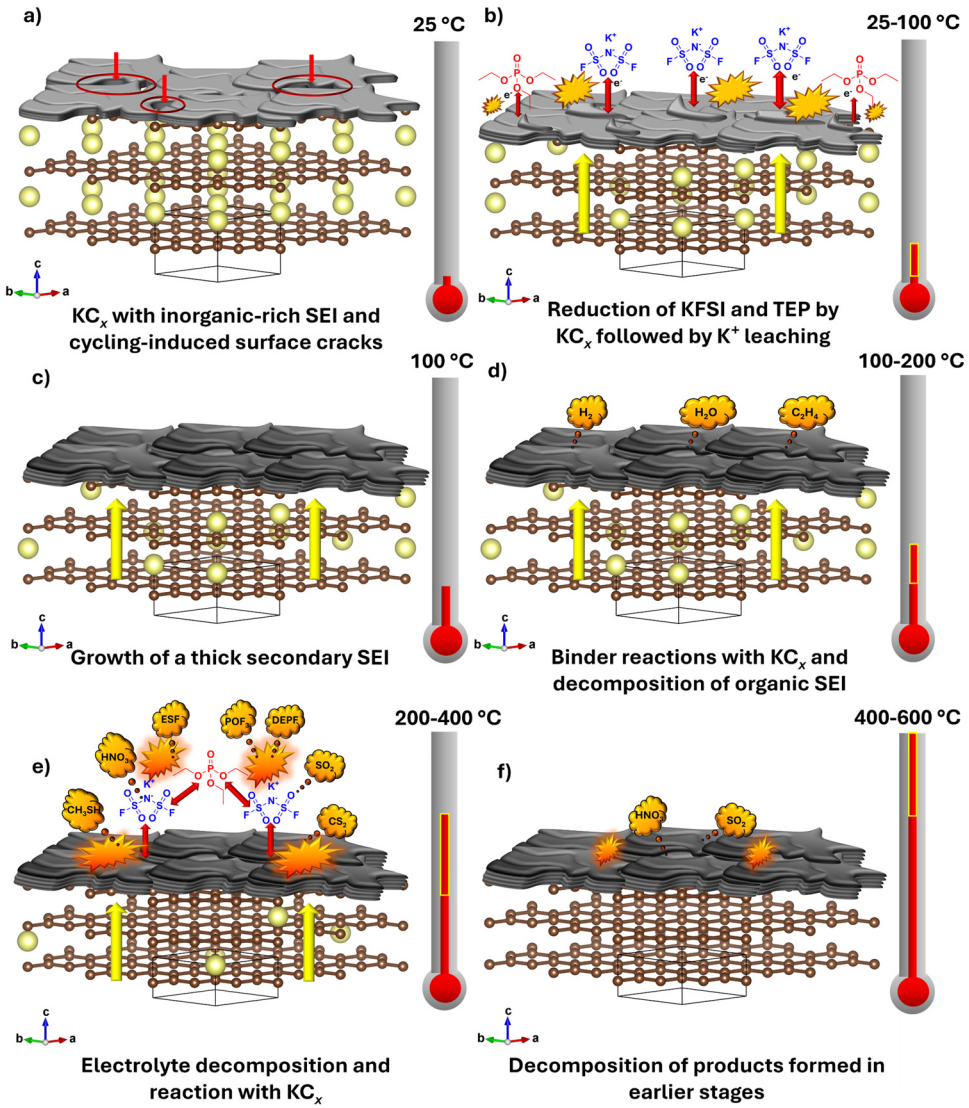

Fig. 3 (a)–(f) Proposed stepwise thermal degradation pathway for the potassiated graphite anode in the 2.5 M KFSI in TEP electrolyte over 25 °C to 600 °C.

graphite.[18] At the anode surface, the highly reactive potassiated graphite reduces KFSI salt, forming relatively thermally stable inorganic materials with leached potassium (*e.g.*, KF, K_xPO_yF). In addition, potassiated graphite can partially react with the TEP solvent and/or the binder, leading to reductive decomposition of TEP and binder, which is responsible for <1% mass loss and slight evolution of CO/C_2H_4 and H_2O. However, the KFSI-potassiated graphite reaction is so fast that its product rapidly passivates the anode surface, blocking further reactions between the anode and KFSI, and TEP, and binder. The above process leads to the formation of a secondary inorganic-rich layer as illustrated in Fig. 3c.

2. Moderate-temperature reactions (100–200 °C): in this temperature range, a small and broad exothermic peak is observed, accompanied by the release of a small amount of H_2, H_2O and CO/C_2H_4 (corresponding to ~7% mass loss). This gas evolution could be associated with reactions between the binder and potassiated graphite and may also result from the thermal decomposition of products from TEP's reaction with potassiated graphite (*e.g.*, $(C_2H_5O)_2PO(OK)$) (Fig. 3d).

3. Elevated-temperature reactions (200–400 °C): the major exothermic thermal reactions occur after ~250 °C, where electrolyte decomposition leads to the generation of gases such as ESF, DEFP, and SO_2, as previously discussed. Additional gases like CS_2 and CH_3SH, which contain carbon and sulfur in lower oxidation states (*e.g.*, +4 in SO_2 *vs.* −2 in CS_2 and CH_3SH), could result from thermal reduction reactions of FSI-related species with remaining partially potassiated graphite (as carbon and electron source), or (ii) gases released during the decomposition of the secondary inorganic-rich layer and the binder.[65] This step is represented in Fig. 3e.

4. High-temperature reactions (400–600 °C): at this stage, the two major exothermic peaks observed could correspond to the thermal decomposition of the components (*e.g.* K_2S_2, $K_2S_2O_3$, polymerized sulfur species (S_x), and possibly small amounts of partially decomposed KFSI residues) that resulted from KFSI decomposition in the previous stage, leading to the generation of gases such as SO_2 and HNO_3 at ~400 °C (corresponding to 2.5% mass loss), followed by another exothermic solid-state reaction at ~500 °C (Fig. 3f). This high temperature region has thermal and gas release behavior similar to that of pure KFSI salt in the same region, reinforcing the idea that the thermal event in this region originates from the thermal decomposition of the intermediates produced during the 200–400 °C stage.

2.3. Thermal behavior of the solid electrolyte interphase (SEI)

Building on previous discussions, which showed that KFSI activates TEP to generate reactive P- and F-containing species above about 200 °C and that fully potassiated graphite anode exhibits an early 65 to 80 °C interfacial exotherm that self-terminates as an inorganic-rich layer forms, we now examine the thermal behavior of the SEI.[61] To identify its key constituents and their thermally driven reconstruction and decomposition, we used two complementary techniques. X-ray photoelectron spectroscopy (XPS) probes the elemental and bonding chemistry of the outer SEI with a sampling depth of less than 7 nm (Fig. 4a–c). Time-of-flight secondary ion mass spectrometry (ToF-SIMS) provides depth-resolved chemical profiles and spatial maps across the full SEI thickness of about 0 to 60 nm. A representative TEM image of a fully potassiated graphite anode at 25 °C (Fig. 4d) shows an SEI thickness of about 60 nm, consistent with the ToF-SIMS depth distribution discussed below. To align with the calorimetric regimes identified earlier, SEIs were analyzed on the potassiated graphite anodes heat-treated at 25, 110 and 340 °C.

2.3.1. XPS analysis. To track how SEI constituents evolve with temperature, we performed high-resolution XPS on fully potassiated graphite anodes (100% SOC). Anode samples were heat treated at 25 °C, 110 °C, and 340 °C in an Ar glovebox (10 °C min^{-1}, 10 min hold) and then transferred into an airtight holder to the XPS chamber (Fig. S18). The 110 °C treatment targets the low-temperature exotherm near 75–80 °C, while the 340 °C treatment targets the higher-temperature window with overlapping exotherms between 240 and 320 °C observed by TGA-DSC (Fig. S14a). By analyzing samples treated at different temperatures, we aimed to capture the progression of SEI restructuring and the chemical transitions of key surface species in the absence of direct electrolyte involvement. This dataset provides a foundational understanding of the inherent thermal behavior of the SEI, which can then be contrasted against the more complex scenarios involving full electrolyte–anode interactions discussed earlier. Fig. 4a–c and Fig. S19 show the *ex situ* XPS measurements conducted on fully potassiated graphite anodes (100% SOC) at 25 °C, 110 °C, and 340 °C for C 1s, O 1s, S 2p, F 1s, N 1s, and P 2p spectra. Peak assignments and constraints are summarized in Table S1 with component quantification in Table S2.

In the K 2p XPS spectra of the anode at 25 °C (Fig. S19a), the two peaks at ~292.86 and ~295.64 eV correspond to K $2p_{3/2}$ and K $2p_{1/2}$ spin–orbit components, respectively, and can be attributed to possible compounds such as K–O containing inorganic SEI species and KF. However, due to the overlapping binding energies of these species (K $2p_{3/2}$ peaks for K_2O and KF are located around 292.4–292.8), spectral deconvolution to distinguish among them was not feasible.[66] Upon heating to 110 °C and 340 °C, the K 2p envelope remains essentially unchanged in position and area (Fig. S19a), indicating that a K-rich inorganic framework K–X (X = F, S, N, and O) persists (Fig. 4a–c and Fig. S19).

In the C 1s spectra at 25 °C (Fig. S19b and Table S1), the peaks at 285 eV, 286.10 eV, 286.90 eV, 288.40 eV, 288.60 eV and 289.80 eV have been assigned to C–C/C–H from graphite, C–O containing SEI compounds like ethoxides, C–OH from Na CMC binder, RCO_2Na from the binder, K_2CO_3 as the SEI component and Na_2CO_3 from the binder respectively. On thermal treatment to 340 °C, a progressive decrease in atomic percentage for binder-related components such as C–OH, RCO_2Na and Na_2CO_3 (29.74%, 60.6% and 77.72% respectively) as well as for ethoxides (63.73%) is observed while K_2CO_3 increases (120.47%), suggesting binder decomposition and an SEI that becomes increasingly inorganic-rich upon thermal treatment.

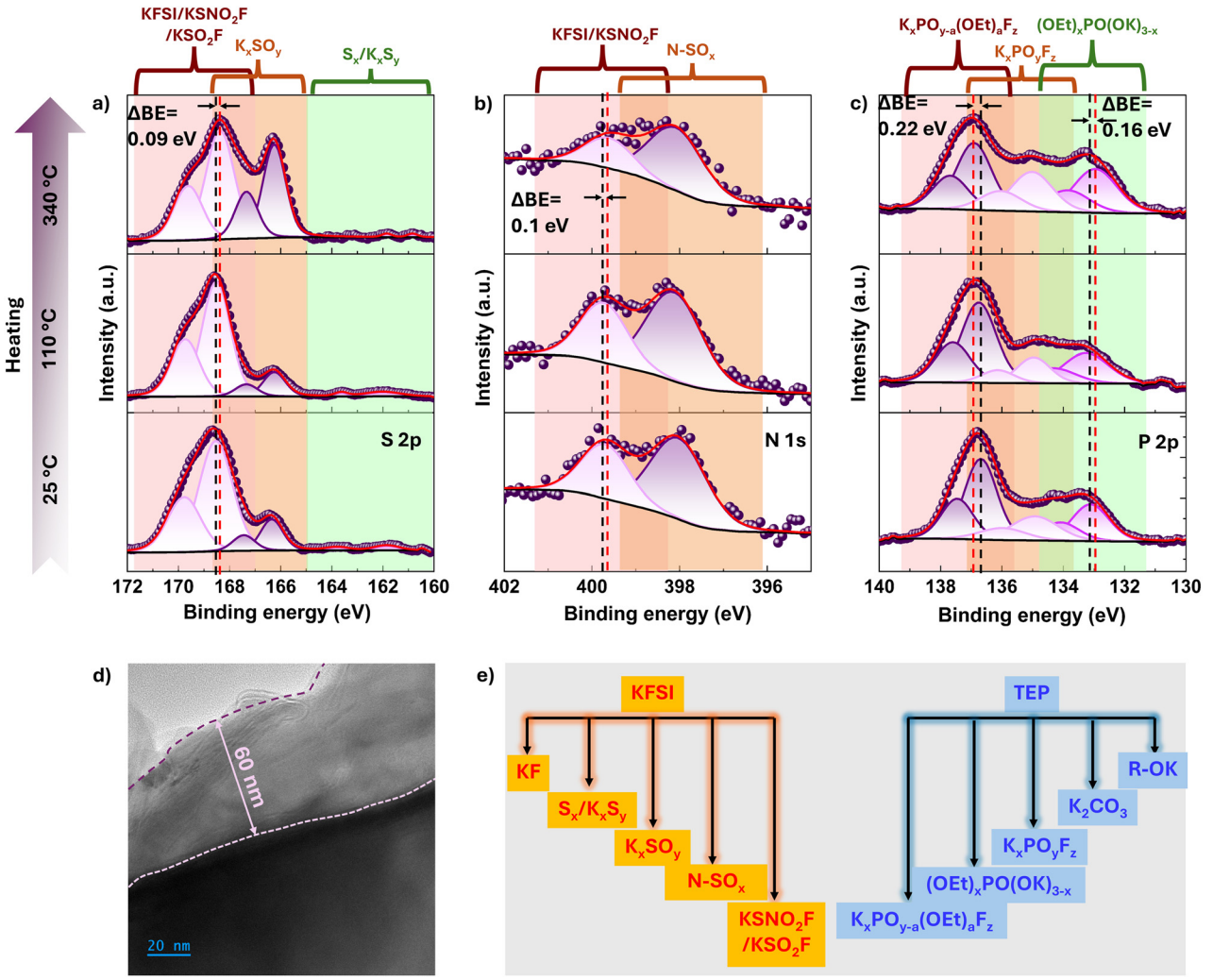

Fig. 4 (a)–(c) XPS spectra showing the interfacial chemistry of anodic decomposition products after the 4th cycle of potassiated graphite (fully charged to 4.3 V *vs.* K/K^+) at three temperatures: at 25 °C (bottom), 110 °C (middle) and 340 °C (top); (a) S 2p, (b) N 1s spectra; (c) P 2p spectra. Binding energy shifts indicate temperature-driven chemical changes. (d) TEM image of the potassiated graphite anode showing a SEI thickness of ~60 nm; (e) proposed electrochemical decomposition of KFSI and TEP contributing to SEI formation during cycling.

Similar results can be observed in the O 1s spectra. At 25 °C (Fig. S19c, Table S1), the observed peaks at 530.40 eV, 531 eV, 531.40 eV, 532.10 eV, 532.70 eV and 533.40 eV have been assigned to K_2CO_3, RCO_2Na/Na_2CO_3, C–O from ethoxides, K_xSO_y-type SEI species, P–O-containing SEI compounds and O═S═O-containing residual KFSI salt and/or partially decomposed KFSI subunits. At 25 °C, based on the atomic percentage (Table S2), the outer SEI seems to have majorly TEP derived organic components (*i.e.* atomic percentage for ethoxides and P–O are 48.91% and 17.37% respectively) and KFSI/KFSI-subunits (atomic percentage ~12.20%). On thermal treatment to 340 °C, a progressive decrease in atomic percentage for RCO_2Na/Na_2CO_3 (56.16%) and ethoxides species (53.2%) is observed while that of K_2CO_3 and K_xSO_y increases (326.39% and 135.89%). Also, atomic percentage for P–O-containing species decreases (67.42%) suggesting P–O bond cleavage. The decrease in atomic percentage for KFSI/KFSI-subunits (45.98%) suggests thermal decomposition of such species in the SEI. All the changes in atomic percentage at 25 °C and 340 °C for each component are listed in Table S2 where a positive sign is % increase and a negative sign indicates % decrease in atomic percentage.

At 25 °C, within the SEI, we assign the high-binding energy (BE) components in O 1s (533.40 eV), F 1s (688.15 eV), N 1s (399.66 eV), and S 2p (168.54 eV and 169.70 eV) to a combination of trapped residual FSI^- and partially decomposed KFSI to smaller products that retain structural motifs of the parent salt, such as $K[NSO_xF_y]$ and $K[SO_xF_y]$ (Fig. 4a, b and Fig. S19c, d, Table S1).[66–68] Upon thermal treatment at 340 °C, these features decrease in intensity, approximately ~46% in O 1s, ~20% in N 1s, and 28.58% in S 2p (Table S2), with a slight shift to lower BEs ($\Delta BE \approx 0.1$ eV). This shift may reflect cleavage of the parent $K[FO_2S–N–SO_2F]$ structure into simpler $K[SO_xF_y]$ and $K[NSO_xF_y]$ fragments. Simultaneously, new lower-BE components emerge in O 1s (530.98 eV) and S 2p (166.38 eV and 167.54), which we assign to $K[SO_x]$, and in N 1s (398.02 eV),

which we attribute to $K[NSO_x]$. These species increase by ~137% ($K[SO_x]$) and ~12% ($K[NSO_x]$), indicating progressive thermal decomposition and/or reduction of $K[SO_xF_y]$, $K[NSO_xF_y]$ or the parent $K[FO_2S–N–SO_2F]$ structure by KC_x. These transformations can suggest they are driven by preferential cleavage of N–S and N–F bonds over the more stable S–O linkages under elevated temperatures.

The peak at 688.15 eV in the F 1s spectrum, previously reported for S–F species (*e.g.*, in KFSI) (Fig. S19d), decreases by 66% after heating to 340 °C (Table S2). This reduction aligns with decreases observed in the S–F component in the S 2p spectrum at 168.54 eV (Fig. 4a) by ~67%. The peaks at 686.42 eV and 687.21 eV have been previously assigned to P–F species.[69,70] In the thermally treated anode sample, P–F species increase by 25.5%, possibly due to the formation of new P–F moieties from the fluorination of phosphate groups which is in line with P–O species decreasing (Fig. S19c). This transformation appears to be driven by thermally induced reactions between potassiated graphite and FSI/FSI-derived intermediates. Moreover, the relative increase in the F 1s signal attributed to P–F over K–F at 340 °C suggests progressive conversion of surface-enriched phosphate groups (corroborated by TOF-SIMS data) into fluoro-phosphate compounds such as $K_xPO_yF_z$.[71]

This interpretation is further supported by the concurrent increase (~24.3%) in the P 2p signal at 134.93 eV and 135.80 eV, which is assigned to mixed fluoro-phosphate phases such as $K_xPO_yF_z$ (Fig. 4c and Table S2). These fluoro-phosphate species may also arise from thermal de-ethoxylation of partially fluorinated organophosphates (*e.g.*, $K_xPO_{y-a}(OEt)_aF_z$), as evidenced by higher-BE features corresponding to P $2p_{1/2}$ and P $2p_{3/2}$ components at 136.69 eV and 137.56 eV, respectively. This reaction is plausibly triggered by thermally activated interactions between potassiated graphite and residual ethoxy-containing phosphate species. At lower binding energies, the P 2p signal can be attributed to organophosphates such as $(C_2H_5O)_2PO(OK)$, which are known to decompose into progressively more potassiated phosphate compounds like $(C_2H_5O)PO(OK)_2$ and $(OK)_3PO$ upon heating from room temperature to 110 and 340 °C. This transformation is accompanied by a systematic shift of the P 2p peaks to lower binding energies, from 133.11 eV at 25 °C to 132.95 eV at 340 °C, consistent with the loss of ethoxy groups and increased K coordination.[72]

Based on the foregoing analysis, a schematic of the resulting SEI chemistry is proposed in Fig. 4e. The SEI is predominantly inorganic, comprising KF, $K[SO_x]$/$K[NSO_x]$ (sulfite/sulfate/sulfonimide–like), fluoro-sulfur oxy species $K[SO_xF_y]$/$K[NSO_xF_y]$, K_2CO_3, Na_2CO_3 (from binder), and K-phosphates/fluorophosphates (K_xPO_y and $K_xPO_yF_z$), with minor reduced sulfides (K_xS_y). A smaller fraction of inorganic–organic/organophosphate species, notably ethoxy-containing phosphates such as $(C_2H_5O)_2PO(OK)$ and related intermediates, exists at 25 °C but diminishes upon heating to predominantly form K_3PO_4 at 340 °C. XPS confirms an inorganic-rich SEI with only minor organic moieties from TEP decomposition and the binder. Upon heating, the high-BE signals associated with KFSI and its subunits diminish, consistent with thermal decomposition and/or reduction by KC_x to form $K[SO_x]$ and $K[NSO_x]$ species, in parallel, phosphate centers become fluorinated, yielding more P–F-containing phases. Moreover, ethoxy phosphates are thermally unstable and convert to more potassiated phosphates, trending toward K_3PO_4.

2.3.2. ToF-SIMS analysis. ToF-SIMS is a powerful, surface-sensitive technique widely used to probe the chemical composition and depth distribution of SEIs in battery electrodes.[73,74] This depth-resolved chemical fingerprinting enables quantification of SEI thickness, component depth localization, and relative comparisons between different SEI components. In this study, ToF-SIMS provides insight into how thermal exposure at 340 °C alters the layering and chemical makeup of the SEI formed on potassiated graphite, compared to the SEI formed during electrochemical cycling at room temperature (25 °C) in 2.5 M KFSI/TEP electrolyte.

To analyze the compositional structure and stratification of the SEI, we examined normalized (to maximum intensity) depth profiles of cycled anodes at 100% state of charge, either dried at 25 °C or thermally treated at 340 °C (Fig. 5a and b). For clarity, only key secondary-ion fragments that mainly relate to various degradation products in the SEI are shown. The C_6^- signal indicates the bulk graphite, and F^-, distributed throughout the entire SEI, was used to estimate the total SEI thickness and help define the location of other fragments. Fragment assignments were made based on chemical families also observed in XPS. Each fragment can originate from multiple parent species: KF^- can arise from KF and KFSI/KFSI-driven products; KCO_3^- from K_2CO_3; KPO^- and PO_2^- from phosphate or fluoro-phosphate species such as K_3PO_4, $K_xPO_{y-a}(OEt)_aF_z$, and $K_xPO_yF_z$; KS^-, KSO^-, and SNO^- from KFSI or its decomposition products including $K[SO_x]$, $K[NSO_x]$, $K[SO_xF_y]$, $K[NSO_xF_y]$, and K_xS_y. A summary of these secondary ion assignments to representative SEI components is provided in Table S3. The assignment of some fragments to KFSI or its electrochemical decomposition products applies only to the sample at 25 °C, whereas in the 340 °C-treated sample, KFSI has fully decomposed into its thermally derived products.

For the 25 °C sample, the ToF-SIMS depth profiles reveal a layered SEI with varying chemical composition. The F^- signal peaks immediately at the outer surface (0–2 nm) and maintains a high intensity throughout the entire SEI (0–64 nm), indicating a consistently high concentration of fluorinated compounds. The outermost SEI (0–6 nm) shows strong signals from SNO^- fragments originating from $K[NSO_x]$, $K[NSO_xF_z]$, and residual KFSI, as well as KCO_3^- (from K_2CO_3) and partially fluorinated or less potassiated PO_2^- species from phosphate or fluoro-phosphate compounds. The PO_2^- fragment peaks near the outer surface, while the KPO^- signal reaches its maximum at deeper layers (>6 nm), suggesting that PO_2^- primarily arises from TEP or less potassiated compounds such as organic derivatives like $(C_2H_5O)_2PO(OK)$ and $(C_2H_5O)PO(OK)_2$. This assignment is further supported by similar normalized depth profiles for $C_2H_3O^-$ and PO_2^-, both mainly concentrated in the outer SEI layer (<6 nm) (Fig. S20). The mid-SEI region

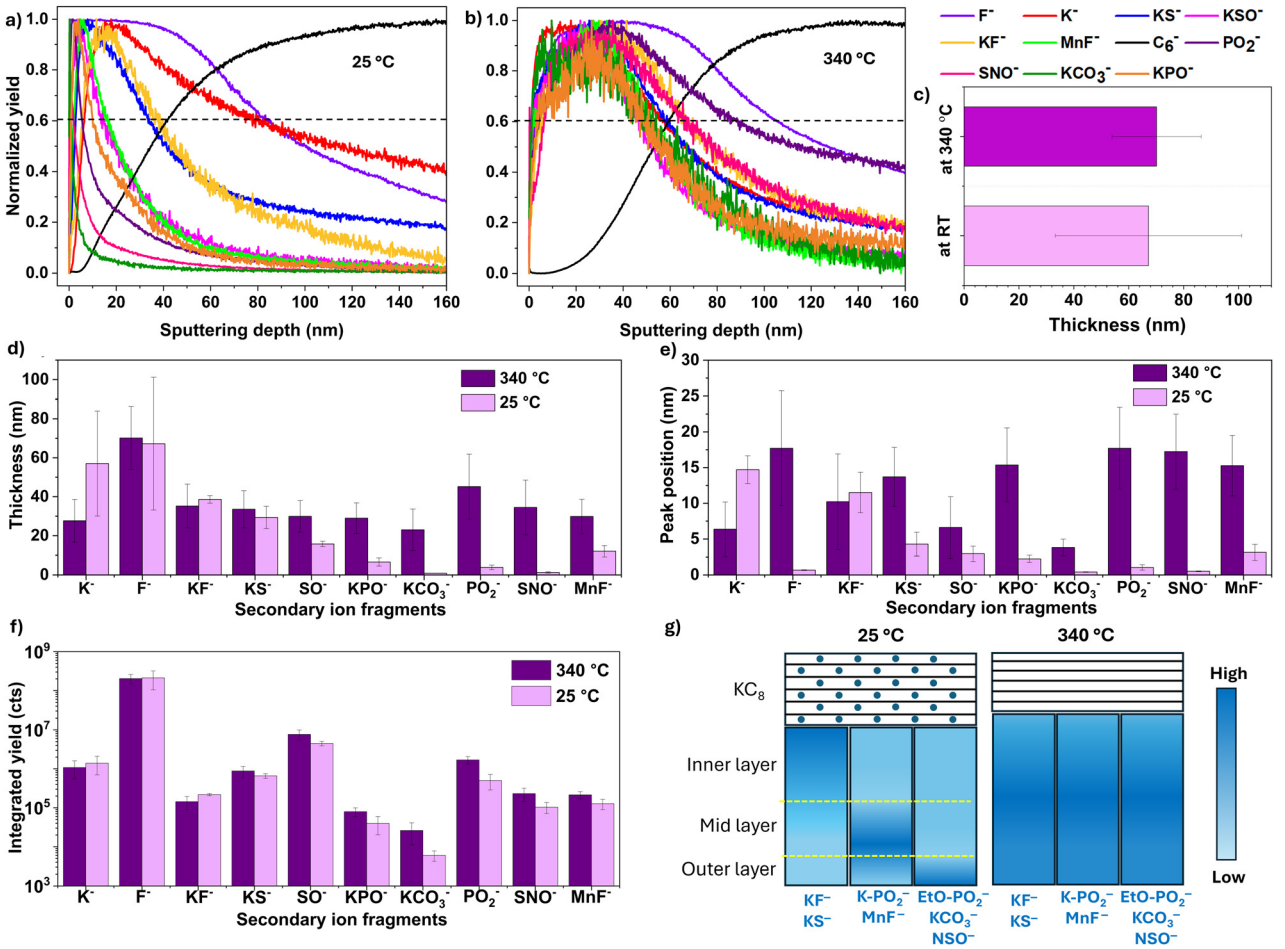

Fig. 5 ToF-SIMS analysis of the SEI formed on potassiated graphite anodes (100% SOC) cycled in 2.5 M KFSI in TEP, comparing samples analyzed at 25 °C and 340 °C. (a) and (b) Normalized depth profiles of selected secondary-ion fragments; (c) comparison of the total SEI thickness at 25 °C and 340 °C; (d) fragment-specific SEI thicknesses; (e) peak positions (depths) of selected fragments; (f) integrated signal intensities of secondary-ion fragments, normalized to the bulk C_6^- signal; (g) schematic illustration of SEI structural reorganization on thermal treatment, showing redistribution of key SEI components (as inferred from ToF-SIMS fragment profiles).

(6–20 nm) is marked by peak intensities of KSO^- and KPO^- fragments, which may derive from multiple sources, primarily $K[SO_x]$, $K[SO_xF_z]$, and K-rich phosphate domains such as K_3PO_4 and fluoro-phosphates. The appearance of the KPO^- signal closer to the anode surface compared to PO_2^- suggests that phosphate species derived from TEP decomposition become more potassiated, likely due to reactions with the highly reactive potassiated graphite surface. In this mid-SEI region, MnF^- is also detected, indicating Mn^{2+} crossover from the cathode,[62] followed by its deposition as MnF_2 or MnS. XPS was not able to detect any Mn signals as the Mn compounds were buried below the penetration depth of XPS (~5 nm). We also checked whether Mn dissolution is accompanied by cyanide dissolution from the PBA cathode. However, our Raman analysis of the anode and electrolyte collected from the cycled full cell (graphite anode/2.5 M KFSI in TEP electrolyte/PBA cathode) showed no –C≡N signal (Fig. S21). The inner SEI layer (20–60 nm), in direct contact with the graphite anode, is dominated by KF^- and KS^- signals, reflecting the accumulation of inorganic KF and reduced sulfur species such as K_xS_y. Similar trends have been reported for Li metal anodes cycled in LiFSI-based electrolytes, where the inner SEI is composed primarily of LiF.[75] This observation suggests that the inner SEI is dominated by KFSI-driven products and lacks phosphorus-rich compounds, indicating that KFSI reacts more readily with the potassiated anode during the initial stages of SEI formation. This results in the formation of the inner SEI layer first, followed by slower TEP decomposition whose products peak in the mid-SEI region.

After thermal treatment at 340 °C, the depth profiles of SEI fragments exhibit broader distributions with greater overlap (except for K^- fragment), indicating spatial homogenization of the SEI components (Fig. 5b). The overall SEI thickness, determined using a cutoff of 0.60 for the F^- signal (the thickest SEI species), increases slightly from 64 ± 34 nm (n = 3) to 68 ± 16 nm (n = 3), as shown in Fig. 5c. This value represents the average thickness measured at three different locations on the sample. The depth profile displayed corresponds to one representative location, where the SEI thickness is 80 nm for the 25 °C sample and 100 nm for the 340 °C-treated sample, based

on the intersection of the F^- signal with the 0.6 intensity line. These values are reflected as the maximum error bars in Fig. 5c. The calculated SEI thickness, the peak-depth positions, and the integrated yields of selected ion fragments before and after heat treatment are summarized in Fig. 5d–f, while changes in SEI stratification upon thermal treatment are illustrated schematically in Fig. 5g. To further illustrate the thermally induced changes in SEI stratification, 3D renderings of the depth profiles for selected SEI fragments are presented in Fig. 6.

Lithium leaching from Li-intercalated graphite upon heat treatment has been previously observed using operando XRD, where the conversion from LiC_6 to LiC_{12} indicates Li^+ diffusion out of the graphite bulk.[18,64] However, this technique does not reveal the destination of the migrating Li^+ ions. Herein, our ToF-SIMS analysis directly visualizes the spatial localization of K^+ relative to the graphite matrix. As shown in the 3D renderings in Fig. 6a, at room temperature, the K^- fragment (represented by the thermal color scale) is deeply embedded within the C_6^- matrix (grey color scale), as evidenced by the substantial overlap in their depth profiles, which points to a thick potassiated graphite layer. The highest intensity of K^- (bright yellow/red) is concentrated in the SEI layer (~0–60 nm), where there is minimal C_6^- signal, while the strongest C_6^- intensity (light grey) lies deeper in the bulk, representing pristine graphite. This behavior is consistent with the depth profiles in Fig. S22. After thermal treatment at 340 °C (Fig. 6b and Fig. S22), the K^- signal diminishes significantly in the graphite surface and increases toward the SEI layer, where C_6^- is absent. This indicates that K^+ has migrated from the graphite surface towards the SEI, where it likely reacts with electrochemically

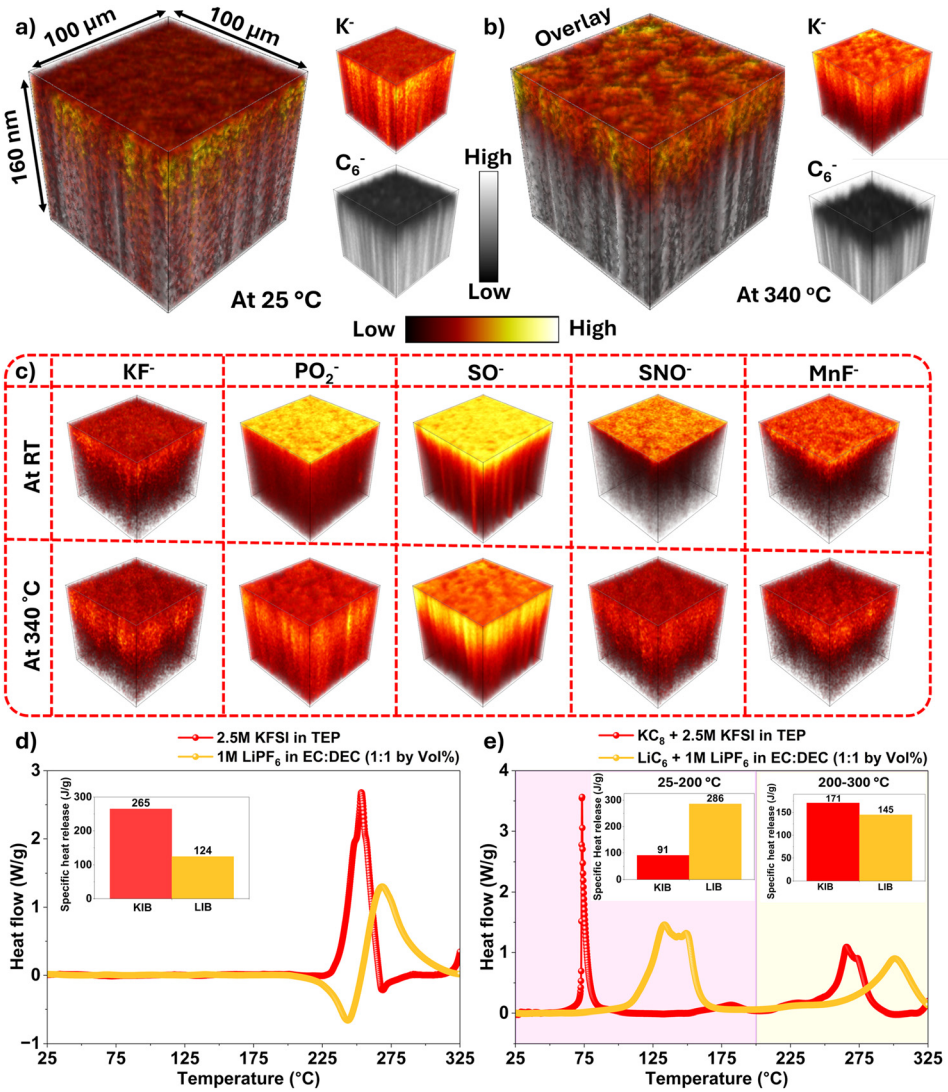

Fig. 6 3D renderings of the ToF-SIMS depth profiles of K^- and C_6^-, along with their spatial overlay, on the surface of potassiated graphite anodes at (a) 25 °C and (b) 340 °C, consistent with K^+ leaching from KC_8; (c) 3D renderings of selected SEI fragments at both temperatures, highlighting changes in spatial distribution upon thermal treatment (see Fig. S23 for the corresponding 2D total ion yield maps of the selected fragments); HP-DSC comparison of thermal behavior in Li-ion and K-ion systems for (d) electrolyte-only samples and (e) anode–electrolyte combinations (in both cases, the anodes were electrochemically cycled in their respective electrolytes: KC_8 in 2.5 M KFSI in TEP and LiC_6 in 1 M $LiPF_6$ in EC:DEC (1 : 1 by vol%).

formed SEI (from the 25 °C sample) or its thermally decomposed products, binder, or carbon defects.

Furthermore, the K^- ion fragment thickness, associated with intercalated potassium, decreases from 58 nm to 28 nm after thermal treatment, and its peak concentration shifts from 0–16 nm (for the sample at 25 °C) to 0–7 nm (Fig. 5d and e). This indicates that leached potassium ions have migrated toward the outer surface. However, as shown in Fig. 5f, the total integrated yield of the K^- signal over the full 160 nm depth (measured as the area under the depth profile curve between the 60% intersections, discussed in previous reports)[75] does not change significantly after heating. Since the K^- signal reflects the total mass of potassium-containing species, this suggests that the leached K ions are retained within the SEI. A direct comparison between the C_6^- and K^- depth profiles shows that, at 25 °C, their strong overlap points to a thick intercalation zone consisting of KC_8. After thermal treatment, the depth profiles for K^- and C_6^- no longer overlap, confirming that potassium ions have been leached from the graphite surface through concurrent reactions of KC_8 with surrounding SEI species. A similar analysis of important SEI fragments is shown in Fig. 5d–f and 6c. At 25 °C, although the F^- signal spans the full SEI thickness (~64 nm), its maximum peak-depth position (MPDP) occurs at 0–2 nm, indicating that fluorine-rich species are concentrated at the outermost interface. The SNO^- and PO_2^- signals also span the outer 0–6 nm region, with MPDPs near the surface (<2 nm), overlapping with F^-. This co-localization suggests that these fragments originate from fluorinated sulfur and phosphate species, such as $K[NSO_xF_y]$ and fluoro-phosphates. However, the broader distribution of F^-, extending ~64 nm into the SEI, implies that the interior is enriched in KF. After thermal treatment to 340 °C, the F^- MPDP broadens to ~18 nm, although its total thickness remains extended (~68 nm), indicating a more uniform distribution of fluorine-containing compounds throughout the SEI. Concurrently, the thickness of the PO_2^- and SNO^- signals increase markedly to 45 nm and 35 nm, respectively, with both showing MPDPs around 17–18 nm.

After thermal treatment at 340 °C, an increase in the integrated yield of the PO_2^- fragment is observed (Fig. 5f). Additionally, the co-localization of the PO_2^- signal with F^- deeper within the SEI (Fig. 5d and e), along with their high correlation (Fig. S24, discussed in the following section in more details), suggests that phosphate moieties are predominantly present as fluoro-phosphate species ($K_xPO_yF_z$). The heated sample also shows an increase in the integrated yield of KSO^- and NSO^- (Fig. 5f), which indicates that fluorinated nitrogen–sulfur–oxygen compounds present at room temperature have undergone partial defluorination (*e.g.*, $K[NSO_xF_y] \rightarrow K[NSO_x]$, $K[SO_xF_y] \rightarrow K[SO_x]$), likely driven by thermally induced KC_8 reactions and potassium leaching. This interpretation is supported by our N 1s XPS data (Fig. 4b). In negative-ion ToF-SIMS detection mode, non-fluorinated $K[NSO_x]$ species yield the NSO^- fragment more efficiently than their fluorinated counterparts. This is because the presence of S–F groups leads to high ionization probability for F^-, SO_2F^-, and SOF^- ions, and less for NSO^-. This behavior is consistent with the observed correlation matrix between NSO^-, PO_2^-, and F^- before and after thermal treatment (Fig. S24). The P–F bond formation upon heating was previously observed in our P 2p XPS data, which suggested that thermally leached potassium can react with FSI/FSI-derived species to generate fluoro-phosphate compounds.

A careful interpretation must be applied when comparing XPS data with ToF-SIMS results, particularly regarding integrated yield intensity and depth-resolved localization. For instance, Mn-containing species are primarily concentrated in the mid-SEI region (beyond ~6–7 nm depth) (Fig. 5d and e) and exist at relatively low overall abundance (Fig. 5f), placing them beyond the effective sampling depth of XPS. In contrast, although the total concentration of KCO_3^- fragments (from K_2CO_3) is even lower than that of Mn species (Fig. 5f), their localization in the outermost SEI region (Fig. 5d and e) renders them readily detectable by XPS. A similar case arises for phosphate species: KPO^- fragments originate mainly from the mid-SEI (Fig. 5d and e) and are comparable in abundance, or even slightly less abundant, than MnF^- in ToF-SIMS (Fig. 5f). However, XPS captures these phosphate species more prominently because additional phosphate-related fragments, such as PO_2^-, are concentrated near the SEI surface where XPS sensitivity is highest.

ToF-SIMS correlation matrices provide a powerful multi-dimensional view into the spatial and compositional evolution of SEI layers on thermal treatment.[73,76,77] The net squared deviation (NSD) analysis between the summed yield maps of selected fragments with details presented in the SI (Tables S4–S7) and the calculated relative correlation matrices from NSD (a method developed and reported in a previous study) have been reported in Fig. S24.[78] These correlation matrices capture the degree of spatial co-localization between 10 discussed ion fragments representing key SEI components and interfacial residues. In other words, the correlation matrix serves as a map of spatial overlap, summarizing whether two ion signals tend to originate from the same physical regions of the surface during sputtering and depth profiling. High correlation values, shown as bright regions, suggest that the corresponding chemistries are intermixed or co-reside within the same SEI domain, whereas low-correlation values indicate segregation into distinct regions or layers. Thus, the primary purpose of this analysis is to translate complex, multi-fragment ToF-SIMS data into an intuitive assessment of SEI stratification *versus* homogenization after thermal treatment. Importantly, the fragments and their chemical assignments do not change before and after heating; rather, it is their spatial organization within the SEI that evolves. The relative correlation matrices of the cycled graphite sample at 25 °C and heat treated at 340 °C are shown in Fig. S24. The correlation matrix for the sample at 25 °C reveals a highly stratified SEI structure, consistent with the normalized depth profile analysis described in the previous section. In contrast, after thermal treatment to 340 °C, the correlation matrix undergoes a marked transformation. Nearly all fragment pairs exhibit increased co-localization, reflected by the broader presence of yellow tones across the matrix

(see Fig. S24). The distinct clustering observed for the sample at 25 °C, is replaced by more homogeneous correlation patterns, suggesting that SEI stratification has been disrupted. This observation aligns closely with the depth profile data in Fig. 5 and 6, which shows merging of the previously distinct outer, middle, and inner SEI layers into a single uniform region. The ToF-SIMS correlation analysis provides strong support for the XPS-derived mechanism of fluorine redistribution during thermal treatment. At room temperature, F^- correlates strongly with SNO^- fragments, indicating that fluorine is primarily associated with intact KFSI-derived N–S(O)F moieties. Upon heating to 340 °C, these correlations decrease markedly, suggesting defluorination of the N–S(O)F moieties. This is consistent with XPS observations of diminishing S–F features and a small downshift of lower BEs in the S 2p and N 1s peaks of fluorinated compounds in the sample at 25 °C. In parallel, the correlations of F^- with PO_2^- fragments increase in the 340 °C sample, demonstrating that fluorine is progressively removed from N–S(O)F-containing species followed by fluorination of phosphate groups. The high correlation between PO_2^- and F^- is also supported by an increase of high-BE P–F signals in the P 2p and F 1s XPS signals.

In conclusion, the combined XPS and ToF-SIMS results reveal that the initially stratified SEI (as shown in Fig. 5g, the SEI shows clear layering: surface-rich SNO^-, KCO_3^- and PO_2^-, mid-depth KSO^-/KPO^- components, and inner KF^-/KS^- adjacent to graphite) formed during electrochemical cycling transforms into a more uniform and homogeneous SEI structure upon heating (*i.e.*, the stratification is destroyed and uniform distribution of SEI components is observed which are largely concentrated in the mid-region as shown in Fig. 5g). This transformation is driven by thermally induced reactions of the graphite host, involving both potassium release from KC_8 ($KC_8 \rightarrow K^+ + 8C + e^-$) and surface lattice contraction (Fig. 5g). The released K^+ migrates outward and combines with newly formed anions generated through either reductive decomposition at the KC_8 interface or thermal decomposition within the SEI. As a result, the SEI becomes increasingly potassium-rich, with uniformly distributed chemical species, as evidenced by the higher integrated yield of all K-containing species observed in the sample at 340 °C. Within this reactive environment, defluorination of FSI-derived species and concurrent fluorination of phosphate groups contribute to the evolution of the secondary SEI composition and bonding structure. Although the observed defluorination of N–S(O)F moieties and concurrent fluorination of phosphate groups may not, by themselves, establish a direct causal link to the exothermic events observed in the anode–electrolyte system, they provide chemically specific descriptors of interphase evolution under thermal stress. These observations suggest that thermally resilient interfaces may benefit from (i) limiting the formation of highly thermally labile N–S(O)F-containing environments and (ii) favoring the development of more inorganic fluoride or fluorophosphate-rich passivation domains that immobilize fluorine during heating. In practice, this perspective motivates electrolyte and interphase design strategies that steer initial SEI composition toward thermally persistent inorganic frameworks, for example through controlled salt-derived passivation at moderated concentration and/or targeted phosphate or fluorophosphate-forming additives, while reducing pathways that generate reactive fluorinated sulfur species at elevated temperature.

2.4. Comparative thermal hazard analysis: KIB *vs.* LIB electrolytes and interfaces

2.4.1. Bulk electrolyte decomposition: heat and gas release profiles. With the increasing interest in KIBs, it is essential to evaluate not only electrochemical performance but also thermal safety metrics. The larger ionic radius and higher chemical reactivity of potassium, together with distinct salt-solvent coordination and solvation structures in KIB electrolytes, can yield thermochemical decomposition pathways and specific enthalpy-release profiles that differ fundamentally from those of conventional LIB systems. Accordingly, benchmarking the electrolyte and the intercalated graphite anode in KIBs against their LIB analogues is critical for identifying safety-limiting processes and guiding the design of thermally robust cells.[9] To approximate sealed-cell conditions, we employed high-pressure differential scanning calorimetry (HP-DSC) from 25 to 325 °C. For each sample, we report the net specific enthalpy change (J g^{-1}) by time-integrating the heat-flow signal over temperature, treating exotherms as positive and endotherms as negative (that is, net heat released = exotherms − endotherms). This convention provides a consistent basis for comparing total heat release across KIB and LIB components.

As shown in Fig. 6d, the K-ion electrolyte (2.5 M KFSI in TEP) releases ~265 J g^{-1}, approximately twice that of 1 M $LiPF_6$ in EC:DEC (~124 J g^{-1}). In both electrolytes, the dominant thermal activity occurs between 200 and 300 °C. These results emphasize that although TEP is low-flammable, it does not necessarily translate to low heat release; the phosphate-based KIB electrolyte exhibits a larger integrated exotherm than the carbonate-based LIB electrolyte. To better contextualize these findings within the KIB field, we evaluated a representative KPF_6-based carbonate electrolyte, 0.8 M KPF_6 in EC : DEC (1 : 1 by volume). The standalone electrolyte exhibits a much lower total heat output (~41 J g^{-1}, net endothermic) and a broader decomposition response with an onset above ~250 °C (Fig. S25), indicating that from a bulk electrolyte perspective, 0.8 KPF_6 in EC:DEC is more thermally stable than the 2.5 M KFSI in TEP electrolyte.

We performed a dedicated TGA-FTIR experiment for the quantification of SO_2 and HF gases, which are primarily associated with FSI^- decomposition and secondary reactions in the KFSI–TEP system. The SO_2 profile (Fig. S26a) exhibits a major release event at 250–260 °C (peak ~ 125 ppm) followed by a second broad event at 400–425 °C (peak ~ 65 ppm), whereas HF evolution is delayed to higher temperatures, beginning above ~300 °C and reaching a maximum of ~40 ppm at ~390 °C. Integration over 25–600 °C yields 0.490 mg SO_2 and 0.060 mg HF, corresponding to 4.08 wt% and 0.50 wt% of the initial electrolyte mass (12.01 mg), respectively. Consistent with the proposed radical-mediated pathway, these trends indicate

that concentrated KFSI–TEP generates substantial sulfur-containing gases in the 200–300 °C window where the dominant exotherm occurs, highlighting the coexistence of toxic gas evolution with significant heat release in the concentrated KFSI–TEP system. Notably, this hazard profile differs from our previous gas analysis reports on conventional carbonate electrolytes, 1 M $LiPF_6$ in EC:DEC, in which HF evolution begins at much lower temperature (just above ~100 °C) and reaches substantially higher peak concentrations (~627 ppm near ~300 °C).[79] In comparison, KFSI–TEP produces far lower HF peak levels and shifts HF release to higher temperatures but generates SO_2 at concentrations that can approach or exceed IDLH levels, indicating that gas-management strategies must particularly account for SO_2 in KFSI-based systems. Karl Fischer titration of the as-prepared 2.5 M KFSI in TEP electrolyte shows a water content of 398 ppm. For the TGA-FTIR quantification experiment, 12.01 mg of electrolyte was used, which based on the KF measurement corresponds to approximately 4.78 μg of H_2O, or about 0.265 μmol. Even under a conservative upper-bound assumption that all H_2O reacts with SOF_2, with each H_2O molecule generating two HF molecules *via* SOF_2 hydrolysis, the maximum HF attributable solely to initial moisture is approximately 0.0106 mg. This value is substantially lower than the approximately 0.060 mg HF quantified over the 25 to 600 °C temperature range. These results indicate that HF and HNO_3 formation is not governed solely by initial H_2O impurities, but also involves H_2O generated *in situ* at elevated temperature, for example *via* decomposition of phosphate species.

We also conducted additional HP-DSC measurements on KFSI–TEP electrolytes at three concentrations, 2.5 M, 1.75 M, and 1.0 M (Fig. S26b) to systematically study concentration effects. The results revealed that with decreasing salt concentration, the exothermic heat release, which is primarily attributed to KFSI decomposition and subsequent cross-reactions between salt-derived radicals and TEP-derived decomposition products, decreases substantially (245 J g^{-1} at 2.5 M, 187 J g^{-1} at 1.75 M, and 100 J g^{-1} at 1.0 M). Conversely, the endothermic contribution, primarily associated with TEP decomposition and volatilization, increases and shifts to higher temperatures as the electrolyte progressively approaches the behavior of the neat solvent. Overall, these results indicate that increasing salt concentration creates a solvation environment that enhances electrochemical stability *via* preferential salt-centered coordination, but can also reduce the intrinsic thermal stability of the electrolyte by enabling salt-derived radical-mediated reaction pathways that amplify exothermic heat release.

2.4.2. Anode–electrolyte interfacial thermal reactivity. The most consequential differences emerge when each electrolyte is contacted with its fully intercalated graphite anode. Fig. 6e compares anode–electrolyte interactions. Over 25–325 °C, the KIB anode–electrolyte reaction (potassiated graphite anode in contact with 2.5 M KFSI in TEP) releases ~262 J g^{-1}, which is comparable to the KIB electrolyte alone (~265 J g^{-1}). By contrast, the LIB anode–electrolyte (lithiated graphite anode with 1 M $LiPF_6$/EC:DEC) releases ~431 J g^{-1}, approximately 3.5 times the heat of the LIB electrolyte alone (~124 J g^{-1}). These results indicate that anode–electrolyte reactivity is substantially more heat-amplifying in the LIB system than in the KIB system, even though the KIB electrolyte by itself is more exothermic upon decomposition. Importantly, when examining interfacial reactivity within KIB carbonate electrolytes, a graphite anode electrochemically potassiated to 100% SOC in 0.8 M KPF_6 in EC:DEC and subsequently analyzed by HP-DSC in contact with the same electrolyte still exhibits an early-onset exothermic event below 100 °C, with a peak centered near ~82 °C, demonstrating that the sub-100 °C reaction is not unique to the KFSI–TEP system (Fig. S27). Over 25–325 °C, the total heat release for potassiated graphite in the presence of 0.8 M KPF_6 in EC:DEC is ~140 J g^{-1}, which is substantially lower than that observed for potassiated graphite in the presence of 2.5 M KFSI in TEP (~262 J g^{-1}). This comparison indicates that electrolyte chemistry strongly influences the magnitude and apparent severity of interfacial heat release, while the presence of an early-onset interfacial exotherm appears to be a general feature of potassiated graphite systems.

To distinguish distinct thermal regimes, HP-DSC profiles are partitioned into low-temperature (25–200 °C) and high-temperature (200–325 °C) regions. In the KIBs, the low-temperature exotherm peaks near ~75 °C and totals ~80 ± 3 J g^{-1}, followed by immediate reaction with the electrolyte. This event is self-limiting because the formation of a thermally stable, inorganic-rich secondary SEI rapidly suppresses further anode–electrolyte reaction beyond ~80–100 °C and only 14 J g^{-1} of addition heat is released between 100 and 200 °C from the binder reaction with potassiated graphite and minor inorganic–organic SEI component decomposition. In LIBs, the low-temperature region releases approximately 286 J g^{-1} and is initiated by thermal decomposition of the organic-rich SEI. This decomposition promotes sustained electrolyte reduction and continues until a secondary passivating layer forms, which quenches the reaction near 170 °C.[61] In the high-temperature region, additional heat arises from secondary-SEI decomposition, anode–electrolyte reactions, electrolyte and salt decomposition, and gas-phase reactions, contributing ~171 J g^{-1} in the KIBs and ~145 J g^{-1} in LIBs.

Overall, the LIB's anode–electrolyte reaction releases ~431 J g^{-1}, about 1.64 times that of the KIB's anode–electrolyte reaction (~262 J g^{-1}) under identical HP-DSC conditions. These contrasts suggest different safety priorities: KIB cells can exhibit earlier onset (~70–100 °C) but modest, self-terminating heat release due to rapid formation of an inorganic-rich passivation; LIB's anode–electrolyte reaction tends to display a later onset (~100–175 °C) but much larger integrated heat that is more capable of driving severe thermal excursions if not contained.

To examine how electrochemical cycling history influences the thermal response of the anode–electrolyte interface, we performed additional HP-DSC measurements on a potassiated anode after 50 galvanostatic cycles in 2.5 M KFSI/TEP (Fig. S28). Relative to the freshly cycled electrode tested with added electrolyte after four cycles, the low-temperature exotherm shifts to a higher temperature, to ~96 °C, and increases in

magnitude to ~110 J g^{-1} after 50 cycles. We attribute this temperature shift to progressive SEI growth and densification during extended cycling, which initially limits electrolyte access to the KC_8 surface and delays the onset of interfacial chemistry until partial decomposition or rearrangement of more labile organic SEI components above ~90 °C opens transport pathways for electrolyte to reach potassiated graphite.[1] This observation differs from the early-cycle case, where a more porous or cracked interphase formed during initial KC_8 expansion and contraction permits earlier electrolyte contact and reaction, followed by comparatively limited organic SEI decomposition. After extended cycling, organic SEI decomposition and the anode–electrolyte reaction occur over a more overlapping temperature window, thereby increasing the integrated heat release associated with the low-temperature event. In sum, these results highlight a practical electrochemical–thermal tradeoff; while the more stable interphases formed after extended cycling can delay the onset of low-temperature reactivity, under thermal abuse conditions the same interphase can undergo chemical and morphological reconstruction, thereby opening transport pathways that allow the anode–electrolyte reaction to proceed more vigorously, leading to a larger integrated heat release for the low-temperature event.

While the present study is focused on anode–electrolyte interfacial reactivity rather than full-cell thermal runaway behavior, it is useful to place the early heat release in a practical context. Calorimetric measurements of the anode–electrolyte system with the anode cycled for five cycles show that the first interfacial exotherm initiates at ~65 °C and peaks near ~75–80 °C, well below typical polyolefin separator shutdown temperatures (~130–135 °C). Although the effective thermal mass of a complete cell would reduce the cell-averaged temperature rise from this event, the early onset and localized nature of this interfacial exotherm can act as a pre-heating step that accelerates subsequent decomposition reactions and increases susceptibility to thermal propagation under abuse conditions. In highly localized regions with limited heat dissipation, the associated interfacial temperature rise could place the anode–separator interface within or approaching the temperature regime associated with separator shutdown. After extended cycling (50 cycles), the anode–electrolyte interfacial exothermic event shifts to higher temperature, with a peak near ~96 °C, and becomes more energetic (~110 J g^{-1} compared to ~77 J g^{-1} after early cycling), while still remaining below typical separator shutdown temperatures. This behavior indicates that interphase growth during cycling can initially impede direct electrolyte access to the potassiated graphite surface, delaying interfacial reactions until partial SEI decomposition or rearrangement enables renewed contact. After extended cycling, the anode–electrolyte reaction proceeds over a more overlapping temperature window, producing a larger integrated heat release associated with the low-temperature event. Together, these observations suggest that electrochemical aging can increase the energetic severity of low-temperature interfacial reactions, thereby strengthening their potential impact on separator stability and thermal propagation under abuse conditions.

3. Conclusion

This study demonstrates how multicomponent couplings such as salt–solvent, salt–anode, solvent–anode, and electrolyte–anode together with the anode state of charge govern the thermal response of potassium-ion batteries employing 2.5 M KFSI in TEP with graphite anodes. Our findings reveal that, despite the electrolyte's low flammability and apparent thermal stability, thermal-abuse tolerance is determined by interfacial reactions rather than bulk flammability. Neat KFSI undergoes multistep thermal decomposition starting at ~280 °C, with successive exothermic events up to ~570 °C, evolving SO_2, HNO_3, and SOF_2 and leaving potassium–sulfur/oxysulfur residues. By contrast, neat TEP volatilizes without detectable decomposition under the same conditions; however, in the electrolyte, KFSI polarizes and activates TEP, converting evaporation into salt-driven, exothermic chemistry that generates reactive intermediates. The potassiated graphite anode (*e.g.*, KC_8) initiates a rapid, low-temperature exothermic interfacial reaction with the electrolyte around 65–80 °C. This early event produces a secondary, inorganic-rich interphase comprising KF, K–sulfur/oxysulfur species, and fluoro-phosphate domains, which suppresses further direct attack on the potassiated graphite. As temperature rises, heat release above ~100 °C is dominated by electrolyte/salt decomposition rather than continued anode consumption. Coupled DSC–TGA–MS–FTIR and GC–MS measurements identify SO_2, HNO_3, HF, ESF (m/z = 194, ethane-1,2-disulfonyl difluoride), DEFP (m/z = 101, diethyl fluorophosphate), POF_3, SO_2F_2, C_2H_4, and DEP as major products between ~200 and 350 °C, consistent with FSI-derived radicals/fluorides reacting with TEP-derived fragments followed by secondary gas-phase transformations. SEI characterization by XPS and ToF-SIMS at 25 and 340 °C reveals that heating drives potassium migration from the graphite host into the SEI, defluorination of N–S(O)F species, and progressive fluorination and potassiation of phosphate groups (forming $K_xPO_yF_z$) near the surface of KC_x particles. As a result, the initially stratified SEI formed during electrochemical cycling transforms into a denser, more uniform and potassium-rich interphase. Overall, these results demonstrate that nonflammability alone is not predictive of cell-level thermal behavior. The earliest thermal event is dictated by interfacial chemistry between potassiated graphite and the electrolyte, specifically KC_x-driven reduction of KFSI and TEP, while the inorganic-rich SEI that subsequently develops can temper further interfacial reactivity but does not eliminate mid- to high-temperature salt/solvent decomposition pathways. Practical mitigation should prioritize suppressing sub-100 °C interfacial reactivity while preserving electrochemical performance by engineering the SEI, tuning salt–solvent coordination to moderate FSI activation and selecting appropriate anode binders for next-generation potassium-ion batteries. More specifically, our results motivate co-optimization of (i) salt concentration and solvation structure and (ii) interphase architecture. Lowering bulk salt concentration reduces electrolyte exothermicity, whereas maintaining ''concentrated-like'' coordination locally

via cosolvent or additive engineering, for example fluorinated phosphate cosolvents such as FTEP, may preserve salt-centered passivation at reduced concentration. In parallel, binder selection that improves conformal coverage and mechanical compliance, such as more strongly adhering and flexible polymer binders, can help limit localized electrolyte access to freshly reactive KC_x sites and thereby suppress initiation and propagation of the sub-100 °C event. Finally, a comparative heat-release analysis between KIBs and LIBs leads to the following insight: while the KIB electrolyte generates more heat upon decomposition than LIB electrolyte, the coupled reactions of the anode and SEI with the electrolyte are significantly more exothermic in LiC_6 systems than in KC_8 systems. Thus, electrolyte chemistry alone does not dictate thermal safety; interfacial reactivity and SEI thermochemistry are the decisive factors too.

Author contributions

S. N.: writing – original draft, methodology, data curation, and conceptualization. A. D.: writing – review and editing, methodology, and resources. A. M. Y.: writing – review and editing. S. S. S.: methodology and resources. D. K.: methodology and resources. K. L. H.: methodology and resources. D. P. F.: writing – review and editing and funding acquisition. O. A. E.: writing – review and editing and funding acquisition. H. K.: writing – review and editing, supervision, project administration, funding acquisition, methodology, and conceptualization.

Conflicts of interest

The authors declare no conflicts of interest.

Data availability

All data needed to evaluate the conclusions of this study are provided in the article and the accompanying supplementary information (SI). Supplementary information is available. See DOI: https://doi.org/10.1039/d5ee06908d.

Additional data that are not available online can be obtained from the corresponding author upon reasonable request.

Acknowledgements

This work is supported by the US DOE Advanced Research Projects Agency-Energy (ARPA-E) JOULES program (award number DE-AR00001723, work authorization number 22/CJ000/07/03). We thank technology manager, H. Cheeseman, for their support throughout this project. The National Renewable Energy Laboratory is operated by Alliance for Sustainable Energy under Contract No. DE-AC36-08GO28308 for the U.S. Department of Energy. The views expressed in the article do not necessarily represent the views of the DOE or the U.S. Government. The U.S. Government retains and the publisher, by accepting the article for publication, acknowledges that the U.S. Government retains a nonexclusive, paid-up, irrevocable, worldwide license to publish or reproduce the published form of this work, or allow others to do so, for U.S. Government purposes. The authors gratefully thank Lingmin Lin for his help with FTIR characterization.

References

1 S. Dhir, J. Cattermull, B. Jagger, M. Schart, L. F. Olbrich, Y. Chen, J. Zhao, K. Sada, A. Goodwin and M. Pasta, *Nat. Commun.*, 2024, **15**, 7580.
2 Z. Tai, Q. Zhang, Y. Liu, H. Liu and S. Dou, *Carbon*, 2017, **123**, 54–61.
3 X. Min, J. Xiao, M. Fang, W. A. Wang, Y. Zhao, Y. Liu, A. M. Abdelkader, K. Xi, R. V. Kumar and Z. Huang, *Energy Environ. Sci.*, 2021, **14**, 2186–2243.
4 Z. Jian, W. Luo and X. Ji, *J. Am. Chem. Soc.*, 2015, **137**, 11566–11569.
5 A. Eftekhari, *J. Power Sources*, 2004, **126**, 221–228.
6 W. Luo, J. Wan, B. Ozdemir, W. Bao, Y. Chen, J. Dai, H. Lin, Y. Xu, F. Gu and V. Barone, *Nano Lett.*, 2015, **15**, 7671–7677.
7 V. Etacheri, R. Marom, R. Elazari, G. Salitra and D. Aurbach, *Energy Environ. Sci.*, 2011, **4**, 3243–3262.
8 A. Yoshino, *Angew. Chem., Int. Ed.*, 2012, **51**, 5798–5800.
9 C. Yang, A. Singh, X. Pu, A. Mallarapu, K. Smith, M. Keyser, M. R. Haberman, H. Khani, P. Misztal and R. Spray, *Nature*, 2025, **645**, 603–613.
10 K. Liu, Y. Liu, D. Lin, A. Pei and Y. Cui, *Sci. Adv.*, 2018, **4**, eaas9820.
11 S.-M. Bak, E. Hu, Y. Zhou, X. Yu, S. D. Senanayake, S.-J. Cho, K.-B. Kim, K. Y. Chung, X.-Q. Yang and K.-W. Nam, *ACS Appl. Mater. Interfaces*, 2014, **6**, 22594–22601.
12 Y. Zheng, Z. Shi, D. Ren, J. Chen, X. Liu, X. Feng, L. Wang, X. Han, L. Lu and X. He, *J. Energy Chem.*, 2022, **69**, 593–600.
13 C. Shi, Z. Li, M. Wang, S. Hong, B. Hong, Y. Fu, D. Liu, R. Tan, P. Wang and Y. Lai, *Energy Environ. Sci.*, 2025, **18**(7), 3248–3258.
14 Y. Yin, Y. Yang, D. Cheng, M. Mayer, J. Holoubek, W. Li, G. Raghavendran, A. Liu, B. Lu and D. M. Davies, *Nat. Energy*, 2022, **7**, 548–559.
15 M. Drüe, M. Seyring, A. Kozlov, X. Song, R. Schmid-Fetzer and M. Rettenmayr, *J. Alloys Compd.*, 2013, **575**, 403–407.
16 A. Du Pasquier, F. Disma, T. Bowmer, A. Gozdz, G. Amatucci and J. M. Tarascon, *J. Electrochem. Soc.*, 1998, **145**, 472.
17 O. Haik, S. Ganin, G. Gershinsky, E. Zinigrad, B. Markovsky, D. Aurbach and I. Halalay, *J. Electrochem. Soc.*, 2011, **158**, A913.
18 X. Liu, L. Yin, D. Ren, L. Wang, Y. Ren, W. Xu, S. Lapidus, H. Wang, X. He and Z. Chen, *Nat. Commun.*, 2021, **12**, 4235.
19 L. Fan, H. Xie, Y. Hu, Z. Caixiang, A. M. Rao, J. Zhou and B. Lu, *Energy Environ. Sci.*, 2023, **16**, 305–315.
20 H. Jia, Y. Xu, X. Zhang, S. D. Burton, P. Gao, B. E. Matthews, M. H. Engelhard, K. S. Han, L. Zhong and C. Wang, *Angew. Chem., Int. Ed.*, 2021, **60**, 12999–13006.

21 H. Jia, Z. Yang, Y. Xu, P. Gao, L. Zhong, D. J. Kautz, D. Wu, B. Fliegler, M. H. Engelhard and B. E. Matthews, *Adv. Energy Mater.*, 2023, **13**, 2203144.
22 R. A. Adams, A. Varma and V. G. Pol, *J. Power Sources*, 2018, **375**, 131–137.
23 S. Liu, J. Mao, Q. Zhang, Z. Wang, W. K. Pang, L. Zhang, A. Du, V. Sencadas, W. Zhang and Z. Guo, *Angew. Chem., Int. Ed.*, 2020, **59**, 3638–3644.
24 J. Wang, Y. Yamada, K. Sodeyama, E. Watanabe, K. Takada, Y. Tateyama and A. Yamada, *Nat. Energy*, 2018, **3**, 22–29.
25 M. Toledo, *Mettler Toledo Thermal Analysis UserCom23*, 2010.
26 K. Kubota, T. Nohira, T. Goto and R. Hagiwara, *Electrochem. Commun.*, 2008, **10**, 1886–1888.
27 L. Schkeryantz, P. Nguyen, W. D. McCulloch, C. E. Moore, K. C. Lau and Y. Wu, *J. Phys. Chem. C*, 2022, **126**, 11407–11413.
28 H.-B. Han, S.-S. Zhou, D.-J. Zhang, S.-W. Feng, L.-F. Li, K. Liu, W.-F. Feng, J. Nie, H. Li and X.-J. Huang, *J. Power Sources*, 2011, **196**, 3623–3632.
29 J. Ding, H. Zhang, W. Fan, C. Zhong, W. Hu and D. Mitlin, *Adv. Mater.*, 2020, **32**, 1908007.
30 Y. Feng, X. Yu, B. Wang, T. Zhang, W. Zhou, Y. Wang, X. Li, J. Zhao, J. Zhao and W. Li, *Angew. Chem.*, 2025, **137**, e202420514.
31 B. Eckert and R. Steudel, *Top. Curr. Chem.*, 2003, **231**, 31.
32 K. Kanayama, H. Nakamura, K. Maruta, A. Bodi and P. Hemberger, *Chem. – Eur. J.*, 2024, **30**, e202401750.
33 A. Mahmood, X. Wang, X. Xie and J. Sun, *Colloids Surf., A*, 2021, **626**, 127058.
34 H. Cheng, Q. Liu, M. Huang, S. Zhang and R. L. Frost, *Thermochim. Acta*, 2013, **555**, 1–6.
35 C. J. Davies, D. A. Newnham and D. M. Smith, *Phys. Chem. Chem. Phys.*, 2003, **5**, 446–450.
36 L. Andrews, V. Bondybey and J. English, *J. Chem. Phys.*, 1984, **81**, 3452–3457.
37 T. A. Blake, C. S. Brauer and C. J. Thompson, *The Infrared Spectroscopy of Equilibrium Mixtures of Vapor-Phase Water and Hydrogen Fluoride*, Pacific Northwest National Laboratory (PNNL), Richland, WA (United States), 2017.
38 M. Xu, L. Han, J. Yan, Y. Geng and C. Guan, The Formation Mechanism and Reaction Pathways of SOF2, SO2F2, SO2 and HF under Local Overheating Fault in SF6 Insulated Power Equipment, 2019 5th International Conference on Electric Power Equipment - Switching Technology (ICEPE-ST), 2019, pp. 618–621.
39 H. Yang, G. V. Zhuang and P. N. Ross Jr, *J. Power Sources*, 2006, **161**, 573–579.
40 W. Weber, V. Kraft, M. Grützke, R. Wagner, M. Winter and S. Nowak, *J. Chromatogr. A*, 2015, **1394**, 128–136.
41 G. Hagele, R. Jüschke, R. Olschner and P. Sartori, *J. Fluorine Chem.*, 1995, **75**, 61–65.
42 R. Jüschke, D. Velayutham and P. Sartori, *J. Fluorine Chem.*, 1997, **83**, 145–149.
43 S. Neupane, R. K. Rahman, A. E. Masunov and S. S. Vasu, *J. Phys. Chem. A*, 2019, **123**, 4764–4775.
44 P. J. Linstrom and W. G. Mallard, *J. Chem. Eng. Data*, 2001, **46**, 1059–1063.
45 O. Ulenikov, O. Gromova, Y. S. Aslapovskaya and V.-M. Horneman, *J. Quant. Spectrosc. Radiat. Transfer*, 2013, **118**, 14–25.
46 L. Daasch and D. Smith, *Anal. Chem.*, 1951, **23**, 853–868.
47 S. M. Aschmann, E. C. Tuazon and R. Atkinson, *J. Phys. Chem. A*, 2005, **109**, 2282–2291.
48 M. C. Zenobi, C. V. Luengo, M. J. Avena and E. H. Rueda, *Spectrochim. Acta, Part A*, 2008, **70**, 270–276.
49 E. Zegers and E. Fisher, *Combust. Sci. Technol.*, 1998, **138**, 85–103.
50 F. Wensink, *Activation of hydrocarbons by gas-phase metal ions*, Sl: sn, 2023.
51 X. Zhang, J. Yan, Y. Zhang, L. Cheng, C. Bian and X. Chen, *IEEE Trans. Dielectr. Electr. Insul.*, 2022, **29**, 1316–1323.
52 M. Alrefae, E.-t Es-sebbar and A. Farooq, *J. Mol. Spectrosc.*, 2014, **303**, 8–14.
53 R. Urlaub, U. Posset and R. Thull, *J. Non-Cryst. Solids*, 2000, **265**, 276–284.
54 J. Zhao, B. Jagger, L. F. Olbrich, J. Ihli, S. Dhir, M. Zyskin, X. Ma and M. Pasta, *ACS Energy Lett.*, 2024, **9**, 1537–1544.
55 Z. Zeng, V. Murugesan, K. S. Han, X. Jiang, Y. Cao, L. Xiao, X. Ai, H. Yang, J.-G. Zhang and M. L. Sushko, *Nat. Energy*, 2018, **3**, 674–681.
56 I. A. Shkrob, T. W. Marin, Y. Zhu and D. P. Abraham, *J. Phys. Chem. C*, 2014, **118**, 19661–19671.
57 G.-F. Zhang, L.-J. Han, C.-F. Guan and C.-R. Ding, *J. Org. Chem.*, 2023, **88**, 13142–13148.
58 J.-i Yamaki, H. Takatsuji, T. Kawamura and M. Egashira, *Solid State Ionics*, 2002, **148**, 241–245.
59 S. Liu, J. Mao, L. Zhang, W. K. Pang, A. Du and Z. Guo, *Adv. Mater.*, 2021, **33**, 2006313.
60 Q. Wang, J. Sun, X. Yao and C. Chen, *J. Electrochem. Soc.*, 2005, **153**, A329.
61 C. Forestier, S. Grugeon, C. Davoisne, A. Lecocq, G. Marlair, M. Armand, L. Sannier and S. Laruelle, *J. Power Sources*, 2016, **330**, 186–194.
62 Y. Shang, X. Li, J. Song, S. Huang, Z. Yang, Z. J. Xu and H. Y. Yang, *Chem*, 2020, **6**, 1804–1818.
63 K. Share, A. P. Cohn, R. E. Carter and C. L. Pint, *Nanoscale*, 2016, **8**, 16435–16439.
64 H. Szeto, V. Kumar and Y. Zhu, *ACS Energy Lett.*, 2024, **9**, 4218–4224.
65 M. C. d S. Farias, W. R. P. d Costa, K. C. Nóbrega, V. B. Romualdo, A. C. A. Costa, R. C. A. d M. Nascimento and L. V. Amorim, *Polymers*, 2025, **17**, 2085.
66 L. Caracciolo, L. Madec and H. Martinez, *ACS Appl. Energy Mater.*, 2021, **4**, 11693–11699.
67 H. Wang, J. Hu, J. Dong, K. C. Lau, L. Qin, Y. Lei, B. Li, D. Zhai, Y. Wu and F. Kang, *Adv. Energy Mater.*, 2019, **9**, 1902697.
68 X. Jiang, X. Liu, Z. Zeng, L. Xiao, X. Ai, H. Yang and Y. Cao, *Adv. Energy Mater.*, 2018, **8**, 1802176.
69 S. Ma, J. Zhao, H. Xiao, Q. Gao, F. Li, C. Song and G. Li, *Angew. Chem.*, 2025, **137**, e202412955.

70 S. Moharana, G. West, A. S. Menon, W. L. da Silva, M. Walker and M. J. Loveridge, *ACS Appl. Mater. Interfaces*, 2023, **15**, 50185–50195.
71 D. Kim, S. Nanda, J. H. Kim, R. S. Monteiro, L. S. Parreira and H. Khani, *J. Mater. Chem. A*, 2025, **13**(6), 4265–4280.
72 Y. Zhu, J. Mou, X. Gong, J. Wang, Q. Feng, X. Sun and Z. Liu, *Fuel*, 2025, **387**, 134456.
73 C. Liu, A. Dolocan, Z. Cui and A. Manthiram, *J. Am. Chem. Soc.*, 2025, **147**(7), 6023–6036.
74 W. Li, A. Dolocan, P. Oh, H. Celio, S. Park, J. Cho and A. Manthiram, *Nat. Commun.*, 2017, **8**, 14589.
75 J. A. Weeks, J. N. Burrow, J. Diao, A. G. Paul-Orecchio, H. S. Srinivasan, R. R. Vaidyula, A. Dolocan, G. Henkelman and C. B. Mullins, *Adv. Mater.*, 2024, **36**, 2305645.
76 T. Ingebrand, Z. Cui, A. Dolocan and A. Manthiram, *Mater. Today*, 2025, **88**, 302–313.
77 R. Sim, L. Su, A. Dolocan and A. Manthiram, *Adv. Mater.*, 2024, **36**, 2311573.
78 B. Jin, A. Dolocan, C. Liu, Z. Cui and A. Manthiram, *Angew. Chem., Int. Ed.*, 2024, **63**, e202408021.
79 L. Lin, A. M. Yanyachi, J. E. Eichler, C. B. Mullins, D. P. Finegan and O. A. Ezekoye, *Energy Storage Mater.*, 2025, 104313.

